Full length article

On the strength–ductility trade-off in thin blast-loaded steel plates with and without initial defects — An experimental study

Benjamin S. Elveli [a,b,*], Mads B. Iddberg [c], Tore Børvik [a,b], Vegard Aune [a,b]

[a] Structural Impact Laboratory (SIMLab), Department of Structural Engineering, NTNU – Norwegian University of Science and Technology, Trondheim, Norway
[b] Centre for Advanced Structural Analysis (CASA), NTNU, Trondheim, Norway
[c] SINTEF Manufacturing AS, Raufoss, Norway

ARTICLE INFO

ABSTRACT

An increase in material strength is commonly associated with better protection in blast-resistant design. However, higher material strength comes at the cost of reduced ductility, and it is still not clear how this trade-off affects the load carrying capacity of blast-loaded structures. This work presents an experimental investigation of the strength–ductility trade-off on the dynamic response of thin steel plates subjected to blast-like loading conditions. Two different plate materials were applied for this purpose; one dual-phase, medium-strength, high-hardening steel, and one martensitic, high-strength, low-hardening steel. Seven plate geometries with various pre-formed defects were tested for both materials, triggering distinctly different deformation and fracture modes in the plates. In total, six different blast intensities were applied, and all tests were recorded using two high-speed cameras synchronized with pressure measurements. 3D-DIC measurements were used to track the mid-point displacement and deformation profile of the target plates until fracture. For plates without defects, the high-strength, low-hardening steel resulted in the smallest deflections for a given load. However, for plates with pre-formed defects, the medium-strength, high-hardening steel showed a superior resistance to fracture. The geometry of the pre-formed defects was found to significantly influence the global deformation, the resistance against crack propagation, and the fracture mode.

1. Introduction

The protection of vital infrastructure against blast or impact loading is still an active field of research (see e.g., [1–5]). In an urban environment, industrial accidents and terrorist attacks both impose threats of explosions in the proximity of civil engineering structures. Such explosions may further result in a combined blast and impact loading, consisting of a blast wave accompanied by fragments [6,7]. Depending on the distance between the point of detonation and the structure, the fragments may impact before, simultaneously, or after the arrival of the blast wave [8]. If the structure is impacted by fragments prior to the blast loading, these fragments may introduce initial damage and perforations, reducing the structural integrity. It has been shown that the combination of these two loads is more critical than the effect of the blast or impact loading alone [9,10]. Despite these observations, such combined loading scenarios are not covered by design codes and few studies are available in the open literature.

Historically, the scope of blast-resistant design has been on massive military structures and government buildings [11]. Concrete structures have therefore been the preferred choice for blast protection,

where concrete slabs exposed to combined blast and fragment loading have been a subject of several studies over the last few decades (see e.g., [12–15]). Leppänen [12] studied concrete blocks exposed to the combination of blast and fragment loading both experimentally and numerically. Bearing balls were glued to explosive charges, and the fragment velocities were measured using an accelerometer and an impact sensor. Grisaro and Dancygier [13] conducted numerical investigations on the dynamic response of a one-way reinforced concrete element exposed to the combination of blast and fragment loading, where the numerical results were validated against experimental and analytical results. Motivated by the potential amplification of damage caused by the interaction between fragment impacts and blast waves, Linz et al. [14] first studied concrete slabs exposed to the combination of a cylindrical explosive charge and ball bearings as fragments before examining the effect of cased explosives on reinforced concrete components for protective structures [15]. It was found that the damage from the combined loading was more severe than for the two cases evaluated separately, which is in good agreement with the findings by Nyström and Gylloft [10].

* Corresponding author at: Structural Impact Laboratory (SIMLab), Department of Structural Engineering, NTNU – Norwegian University of Science and Technology, Trondheim, Norway.
E-mail address: benjamin.s.elveli@ntnu.no (B.S. Elveli).

In contrast, civilian structures are often lightweight and flexible, and the response of thin-walled metallic components are therefore of interest (see e.g., [16–18]). Assuming that the fragments strike before the arrival of the blast wave, Rakvåg et al. [16] investigated the effect of different pre-cut defects in thin square Docol 600DL steel plates subjected to a fast transient pressure loading. The defect shapes were squares, diamonds, slits, and circular holes. All plates had four equal defects symmetrically distributed around the centre, and it was found that the defect shape and area had a significant influence on the maximum deflection. It is however important to notice that the test setup used in Ref. [16] did not result in a blast wave impacting the target plates, but a rapid change in pressure on the two sides of the target plate.

Inspired by the work of Rakvåg et al. [16], the response of Q345 steel plates with different pre-cut holes exposed to a blast load caused by detonating a charge of TNT was studied by Li et al. [19]. The explosive charge was placed at a fixed stand-off distance, while varying the amount of TNT to control the blast intensity. The pre-formed defects were included to imitate the effect of fragment impact prior to the blast loading. Plates with square, circular, and diamond-shaped defects were tested. For the plates with square and circular defects, no fracture was observed for any of the applied blast intensities. On the contrary, all plates with the diamond-shaped defect fractured during testing, and it was concluded that the shape of the defect altered the capacity to fracture.

Aune et al. [20] studied the dynamic response of thin Docol 600DL steel plates subjected to blast loading. The study was conducted using a compressed gas-driven shock tube to generate a controlled and repeatable blast environment [21]. Thin steel plates with and without pre-formed defects were tested. Special focus was placed on the influence of the pre-formed holes on the dynamic response and on the fracture modes of the plates. The study indicated an increase in global displacement for plates with pre-formed holes compared to plates without pre-formed defects under similar loading conditions.

In protective design, a common understanding is that an increased material strength leads to better protection (see e.g., [22,23]). Børvik et al. [24] showed both experimentally and numerically that the ballistic perforation resistance increases almost linearly with the yield stress of the target material, while the dominant indicator for blast resistance of ductile plates is less pronounced in the literature. Both Langdon et al. [25] and McDonald et al. [26] suggested that the specific energy to tensile fracture could serve as an indicator for the fracture resistance, whereas McDonald et al. [26] further showed that high-strength steels could outperform more ductile steels under blast loading.

Increased material strength is typically accompanied by reduced ductility, and this strength–ductility trade-off has been a long-standing dilemma in materials science [27]. Geometrical defects like sharp notches and holes introduced by impacting fragments typically involve stress concentrations and large local plastic deformations upon loading. The presence of these local plastic deformations questions whether ductility could be critical for the protection against combined blast and impact loading. A recent study by Holmen et al. [28] on the perforation resistance of high-strength aluminium plates indicates that even though strength was observed to be the most important parameter for perforation resistance, work hardening and ductility became increasingly important in predicting the fragmentation of the target plate material. Granum et al. [29] carried out experiments and numerical simulations on the blast performance of 1.5 mm thick aluminium plates with four different pre-formed defects. Three different tempers were used to vary the material properties with respect to strength, work hardening, and ductility. It was found that both the fracture mode and the blast performance were sensitive to changes in the number, spatial distribution, and orientation of the pre-formed defects, as well as changes in material properties. These results indicated that the ductility and work hardening were more important for the blast resistance than the strength.

Steel is often preferred in protective structures due to its combination of high strength, high ductility and good formability, resulting in an effective load carrying capability at a relatively low cost compared to many other materials. The mechanical properties of steel result from a combination of chemical composition, heat treatment and manufacturing process. Generally, dual-phase steels are characterized by a microstructure consisting of hard martensitic islands, surrounded by a softer ferrite matrix. The soft ferrite matrix provides high ductility, while the hard martensite contributes to increased strength [30]. An increased proportion of martensite therefore results in a strength–ductility trade-off, leading to an increase in strength while decreasing the ductility of the material.

Motivated by the observed trade-off between material strength and ductility in recent studies [25,28,29], this study provides an unique experimental dataset giving further insight on the strength–ductility trade-off in thin, blast-exposed steel plates. A comprehensive experimental campaign enabled detailed studies on the influence of material strength and ductility on the performance of plates with different initial defects (shape, number and spatial distribution). Two different steel alloys being Docol 600DL and Docol 1400M were chosen to represent medium- and high-strength steels, respectively. The main objectives of this study are: (1) to provide new insight into the importance of the material strength and ductility on the blast performance of thin, plated structures with and without pre-formed defects; and (2) to establish a comprehensive experimental dataset allowing for validation and further development of computational methods in forthcoming studies.

2. Materials

2.1. Materials description

The materials investigated in this study were Docol 600DL and Docol 1400M steels, produced by the Swedish manufacturer SSAB [31]. Both alloys are cold-rolled and available in a thickness range from 0.5 mm to 2.1 mm. Docol 600DL is a dual-phase, medium-strength, high-hardening steel, while Docol 1400M is a martensitic, high-strength, low-hardening steel. These materials are mainly developed for use in the automotive industry. The pure martensitic Docol 1400M material has a yield strength roughly 5 times higher than the dual-phase Docol 600DL (see Table 2), whereas Docol 600DL has about 5 times larger elongation to fracture. The chemical composition and nominal material parameters for both steels are given in Tables 1 and 2, respectively.

2.2. Material testing

Quasi-static tension tests were performed to characterize the mechanical response of the materials at large deformations. For the Docol 600DL material, the test results from Aune et al. [20] were adopted. Quasi-static tension tests of the Docol 1400M material were carried out using an Instron 5982 testing machine at a constant deformation rate of 2.1 mm/min, using the same experimental setup as presented in Ref. [20]. A uniaxial test specimen with a gauge area of 70 mm × 12.5 mm was used (see e.g., Gruben et al. [32] for the specimen geometry), giving an initial strain rate in the material of $\dot{\epsilon}_0 = 5 \cdot 10^{-4} s^{-1}$. To investigate the material anisotropy, tensile specimens were extracted at 0°, 45° and 90° relative to the rolling direction of the plates. A speckle pattern was applied to the surface of the tensile specimens using an airbrush, enabling two-dimensional (2D) digital image correlation (DIC) to obtain the displacement field on the surface of the specimens during the post-processing of the images [33]. Global strains were calculated from the displacement field using a virtual extensometer with an initial length of 60 mm. The force was measured by the load cell of the testing machine and synchronized with images of the specimen surface captured at a sampling rate of 4 Hz.

Table 1
Chemical composition of Docol 600DL and Docol 1400M (in wt.%). The data is taken from [31].

Material	C (max %)	Si (max %)	Mn (max %)	P (max %)	S (max %)	Al (min %)	Nb+Ti (max %)
Docol 600DL	0.10	0.40	1.50	0.010	0.002	0.040	–
Docol 1400M	0.20	0.40	1.60	0.020	0.010	0.015	0.10

(a)   (b)
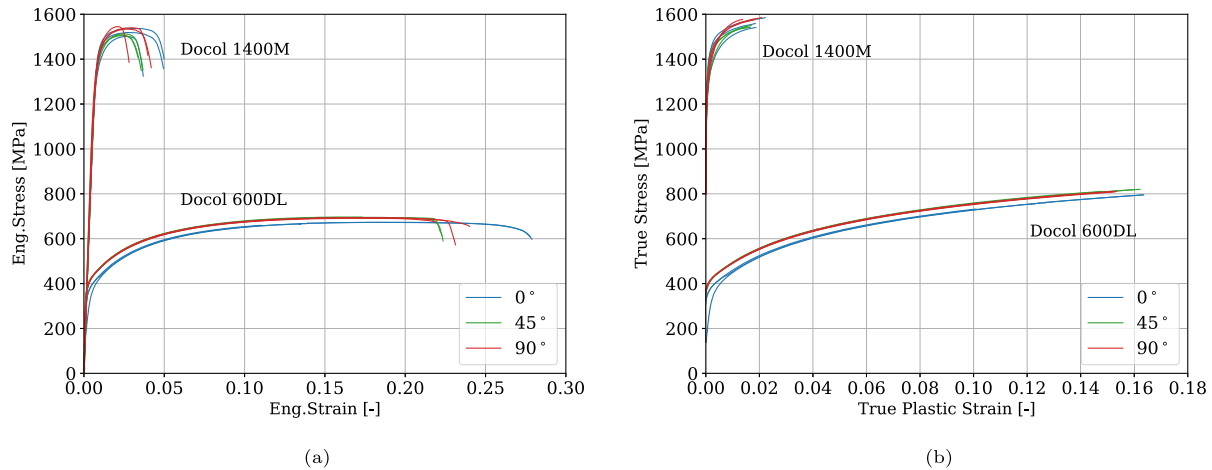
Fig. 1. Stress–strain curves obtained from tension tests of the two materials: (a) engineering stress–strain curves and (b) true stress–plastic strain curve until diffuse necking. *Source:* The curves for Docol 600DL are taken from [20].

Table 2
Nominal material parameters for the two materials under consideration as given by SSAB [31]. Here, E is the elastic modulus, ν is the Poisson's ratio, ρ is the density, σ_y is the initial yield stress, σ_{uts} is the ultimate tensile strength, and ε_{fail} is the elongation to fracture.

Material	E [GPa]	ν [-]	ρ [kg/m^3]	σ_y [MPa]	σ_{uts} [MPa]	ε_{fail} [%]
Docol 600DL	210.0	0.33	7850	280–360	600–700	20
Docol 1400M	210.0	0.33	7850	1150-	1400–1600	3

Fig. 1(a) presents a comparison of the engineering stress–strain curves until fracture, while Fig. 1(b) provides the true stress–plastic strain curves for Docol 600DL and Docol 1400M up to diffuse necking. As expected, significant differences in both strength, work hardening and ductility are observed between the two steels. Docol 600DL yields at about 350 MPa, whereas Docol 1400M yields at roughly 1200 MPa. Furthermore, it is seen that Docol 600DL has approximately 5 times larger elongation to fracture than Docol 1400M when considering the engineering strains. Fig. 1(b) shows that the true stress for Docol 600DL is increased from around 350 MPa at initial yield to just above 800 MPa at the onset of diffuse necking. This corresponds to an increase of about 130% relative to the initial yield stress. Docol 1400M shows an increase in true stress less than 30% from initial yield to diffuse necking. From the true stress–plastic strain curves, it is evident that Docol 600DL undertakes a significantly larger amount of work hardening than Docol 1400M. All observed differences in behaviour for the two materials are in good agreement with the mechanical properties described in Section 2.1.

Fig. 1(a) reveals variations in both flow stress and elongation to fracture for both materials. The degree of deviation between tests appears to depend on the orientation of the tensile specimen relative to the rolling direction of the plate. Tests on specimens oriented 45° relative to the rolling direction showed the least variation both with respect to the stress level and elongation to fracture. The results from tests on specimens in the 0° and 90° orientations appear to experience larger variations. It should finally be noted that the observed variations in the tension tests for this batch of Docol 1400M were comparable to the variations found in tests on similar materials, see e.g., [20,32,34].

3. Experimental study

3.1. Experimental setup

The experiments were performed in the SIMLab Shock Tube Facility (SSTF) at NTNU. A detailed presentation of the SSTF and its performance in generating blast-like loading conditions is given by Aune et al. [21], and will therefore only be presented briefly in this section. The SSTF is designed to create pressure waves in air with similar characteristics as a real blast wave. The facility is equipped with two synchronized high-speed cameras (Phantom v2511) pointed at the target plate as well as pressure sensors located at different locations within the SSTF, allowing for detailed studies of the dynamic response of plated structures. The experimental setup used in this study is shown in Fig. 2.

The propagation of the blast wave is initiated at the driver side of the shock tube and impacts the target plate just inside the tank at the right end of the tube. In this study, all experiments were performed with a driver length of 0.77 m and compressed air was used to pressurize the driver section.

The target plates were mounted to the shock tube by using a clamping assembly. The dimensions of the clamping assembly are given in Fig. 3. All target plates had dimensions of 625 mm x 625 mm x 0.8 mm and a blast-exposed area of 300 mm x 300 mm.

Both the incoming and reflected overpressure were sampled with a frequency of 500 kHz at Sensor 1, see Figs. 2 and 3. Sensor 1 is located 245 mm upstream of the target plates and serves as the best available estimate for the pressure acting on the surface of the target plates. Hence, all pressure histories presented in this study are measured at Sensor 1 and represent the overpressure relative to atmospheric conditions.

Two high-speed cameras were positioned in a stereoscopic setup and used to capture images at a sampling rate of 37 kHz. Prior to each test, the target plates were spray-painted with a black and white speckle pattern, allowing the displacement field to be obtained during post-processing of the image pairs by using the in-house 3D-DIC software eCorr [35]. A common time axis was used for the post-processing, where the time $t = 0$ was set to the time when the incoming pressure wave reached Sensor 1 (see Fig. 3).
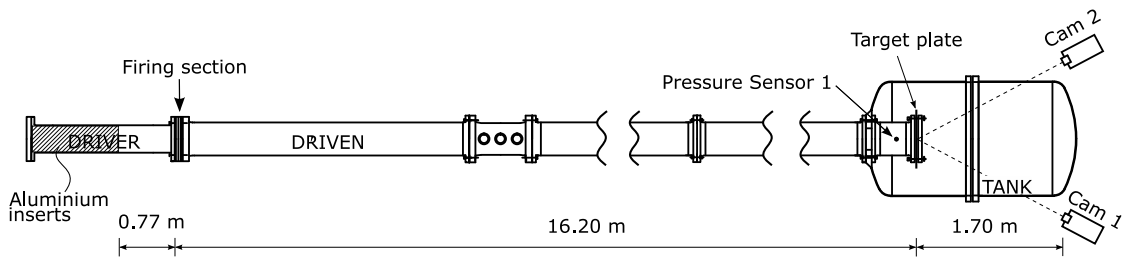
Fig. 2. Illustration of the SIMLab Shock Tube Facility (SSTF), where the pressure sensor used in this study (Sensor 1) is located 245 mm upstream the target plate.
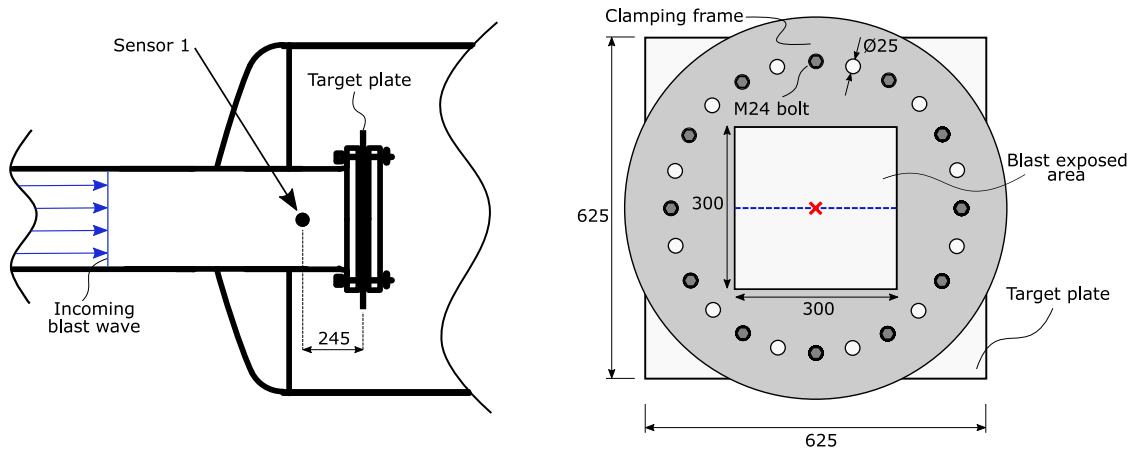

Fig. 3. Clamping assembly in the SSTF: The downstream end of the SSTF (left), where the clamping assembly and pressure sensor (Sensor 1) are located, and a detailed sketch of the clamping assembly including the target plate (right). The red cross at the centre of the blast-exposed surface indicates the sampling point for mid-point displacements, and the blue horizontal line shows the position for the sampling of deformation profiles. (For interpretation of the references to colour in this figure legend, the reader is referred to the web version of this article.)
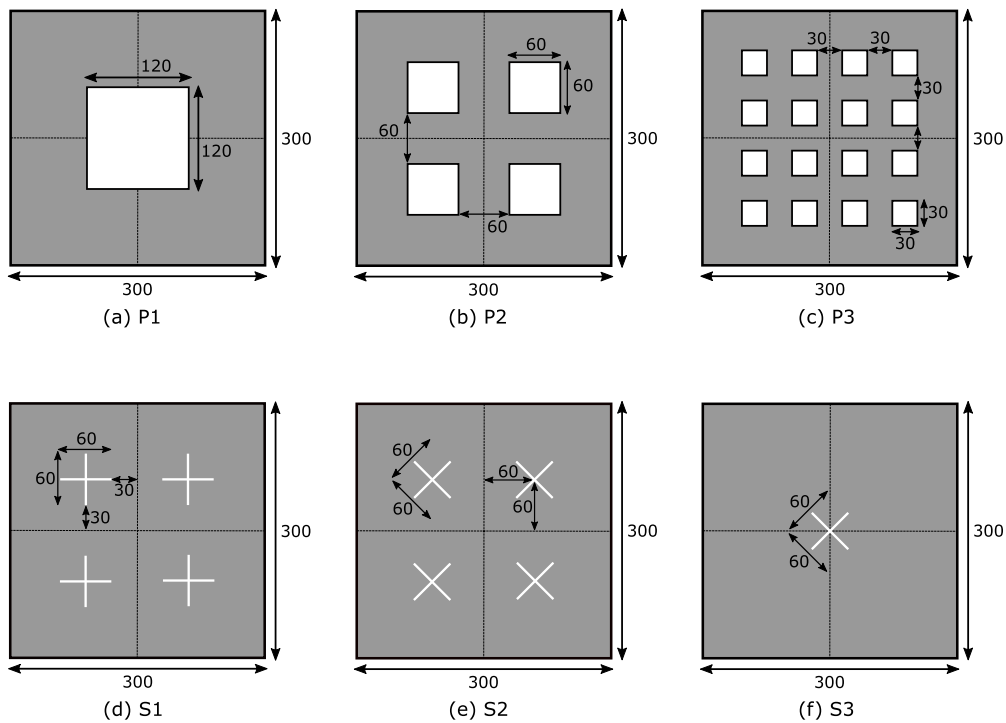

Fig. 4. Geometry of the target plates with pre-formed holes in (a)–(c), named P1, P2, and P3, respectively, and pre-formed slits in (d)–(f), named S1, S2, and S3, respectively.

Table 3
Experimental programme.

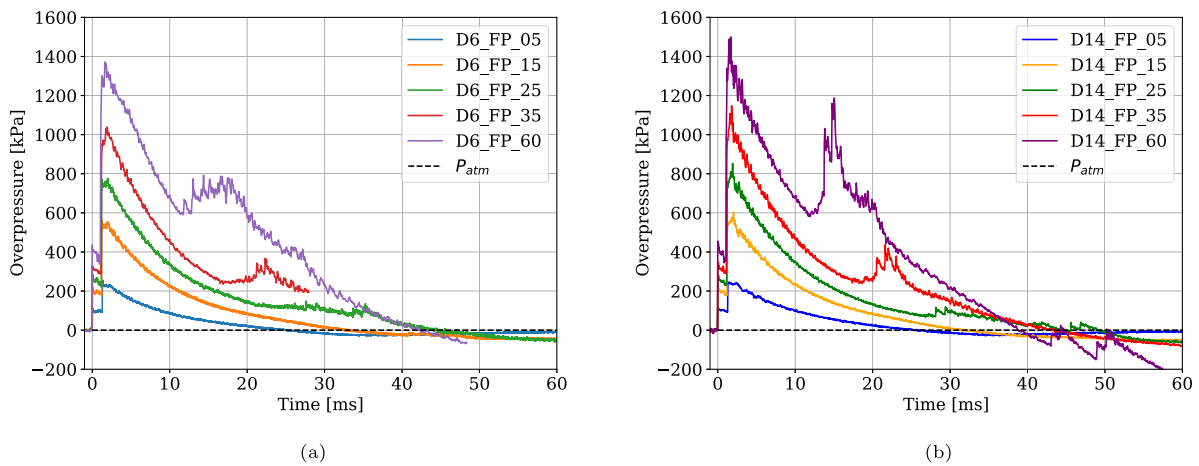| Firing pressure	FP	P1	P2	P3	S1	S2	S3
5 bar	D6_FP_05	D6_P1_05	D6_P2_05	–	D6_S1_05	–	–
	D14_FP_05	D14_P1_05	D14_P2_05	–	D14_S1_05	–	–
10 bar	–	D6_P1_10	–	–	D6_S1_10	D6_S2_10	–
	–	D14_P1_10	–	–	D14_S1_10	D14_S2_10	D14_S3_10
15 bar	D6_FP_15	D6_P1_15	D6_P2_15	D6_P3_15	D6_S1_15	D6_S2_15	–
	D14_FP_15	D14_P1_15	D14_P2_15	D14_P3_15	D14_S1_15	D14_S2_15	D14_S3_15
25 bar	D6_FP_25	D6_P1_25	D6_P2_25	D6_P3_25	–	D6_S2_25	D6_S3_25
	D14_FP_25	–	D14_P2_25	D14_P3_25	–	D14_S2_25	D14_S3_25
35 bar	D6_FP_35	–	D6_P2_35	D6_P3_35	–	–	D6_S3_35
	D14_FP_35	–	D14_P2_35	D14_P3_35	–	–	–
60 bar	D6_FP_60	–	–	–	–	–	–
	D14_FP_60	–	–	–	–	–	–

(a)

(b)

Fig. 5. Pressure histories for the tests on full plates (FP) without any defects: (a) the D6 material and (b) the D14 material.
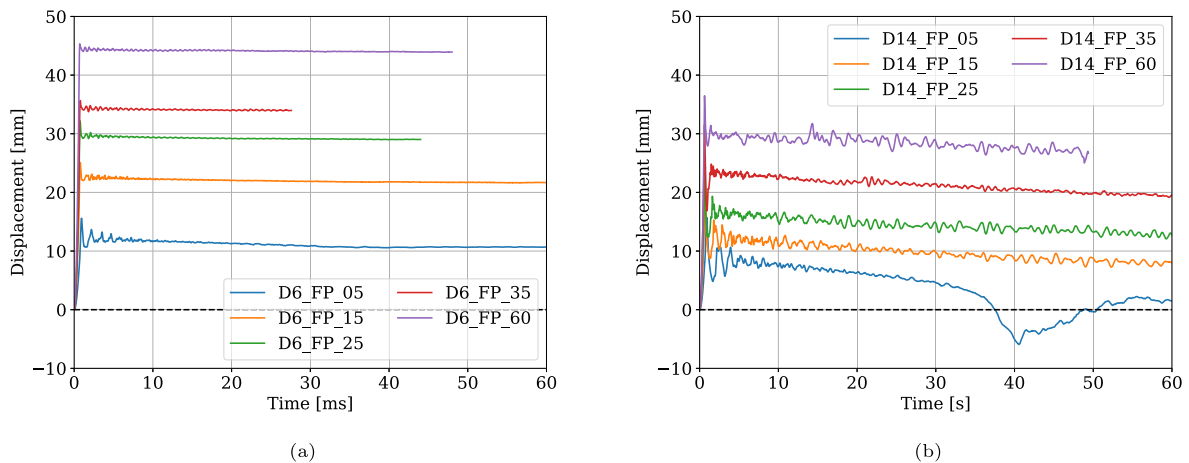

(a)

(b)

Fig. 6. Mid-point displacements versus time for the tests on full plates (FP) for both materials: (a) the D6 plates and (b) the D14 plates.

3.2. Experimental program

The aim of the experimental program was to assess the influence of material strength and ductility on the blast resistance of thin steel plates with various initial geometrical defects. Motivated by the ability to trigger distinct fracture modes, the geometries used in the studies by Aune et al. [20] and Granum et al. [29] were adopted. In addition,

two new plate geometries were used in this study. The geometries under consideration are presented in Fig. 4. While keeping the total hole area constant for all plate geometries, the two new pre-damaged configurations tested in this study had one single square perforation at the centre (P1 in Fig. 4a) and 16 square perforations (P3 in Fig. 4c). These perforations resulted in a 16% reduction of the blast-exposed area.
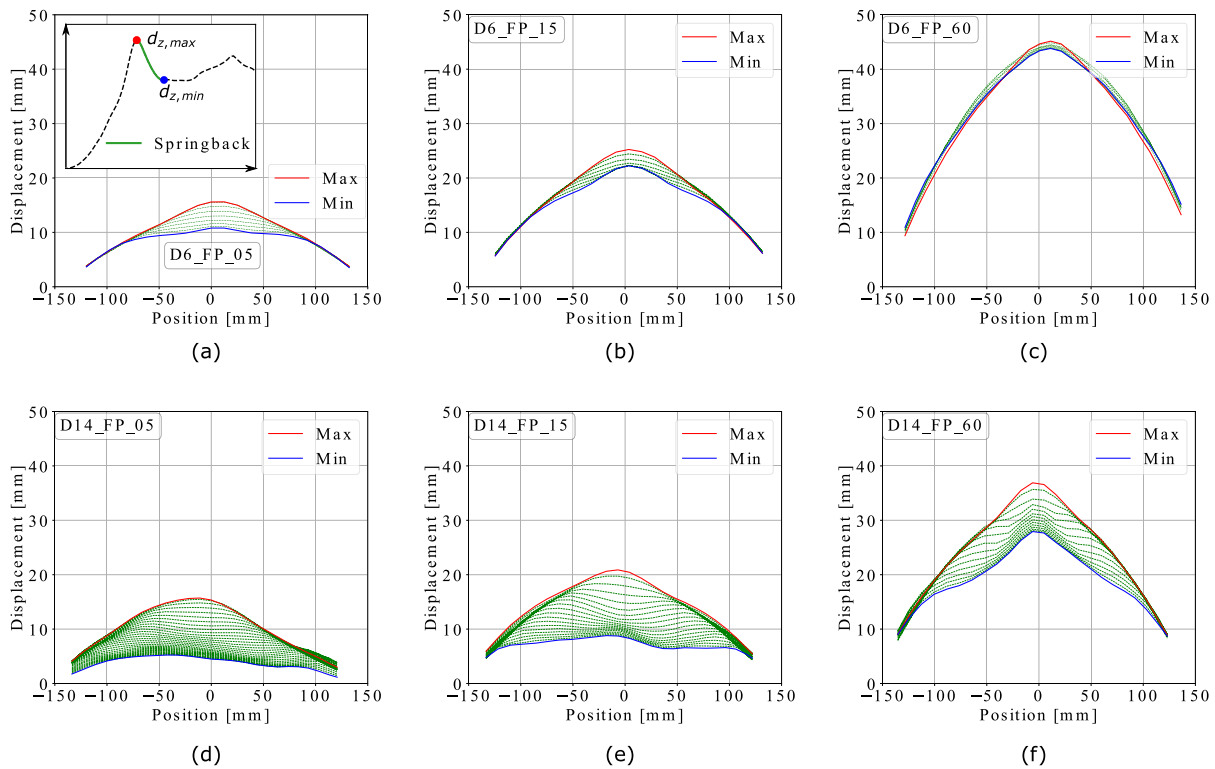
Fig. 7. Deformation profiles at maximum deflection ($d_{z,max}$) represented by red lines and at minimum deflection ($d_{z,min}$) indicated by blue lines: (a) D6_FP_05, (b) D6_FP_15, (c) D6_FP_60, (d) D14_FP_05, (e) D6_FP_15 and (f) D14_FP_60. The green lines show the development of the deformation profile from $d_{z,max}$ to $d_{z,min}$ at a constant sampling rate of $\Delta t = 0.027$ ms. The subplot in (a) indicates the elastic springback on a midpoint displacement curve. (For interpretation of the references to colour in this figure legend, the reader is referred to the web version of this article.)

As ductility is assumed to influence the response of the target plate only in the presence of large plastic deformations, three distinctly different levels of deformations were investigated for each geometrical configuration. These responses were triggered using three distinct load levels, where the blast intensities were controlled by the firing pressures. The lowest blast intensity was intended to result in small plastic deformations, the intermediate pressures should result in large plastic deformations and possible crack initiation, and the highest pressure should result in large plastic deformations with considerable crack propagation and possible complete fracture. For both materials, all geometrical configurations were tested for the same blast intensity for a direct comparison with respect to the overall dynamic response and capacity in resisting the blast load.

The experimental programme is provided in Table 3. Each test is numbered DX_Y_Z, where D denotes deformable steel plate (D), X indicates either the medium-strength Docol 600DL (D6) or the high-strength Docol 1400M (D14). Y represents the plate geometry, i.e., full plate (FP), one hole in the centre (P1), four holes (P2), 16 holes (P3), four slits oriented horizontal and vertical (S1), four slits rotated 45° (S2) with respect to S1, or one rotated slit in the centre (S3). Z indicates the firing pressure in bar in the driver. The blast intensity in the various tests was varied by changing the firing pressure in the driver section of the SSTF. Note that the firing pressures presented in Table 3 are rounded to the lower multiple of 5.

Aune et al. [20] investigated the dynamic response of both full plates (FP) and plates with four pre-formed square holes for Docol 600DL (D6) and the results are adopted and labelled P2 in the present study.

4. Experimental results

The presentation of the experimental results is divided into three main parts. First, the global response of the target plates without holes are presented in Section 4.1. Then, the results from tests on plates with different pre-formed defects are presented in Section 4.2. The global response is evaluated based on the recorded pressure histories and deformations measured by 3D-DIC. Finally, fracture modes and the blast resistance are evaluated for the different geometries and materials in Section 4.3. It is important to emphasize that the presentation of results herein is limited to the representative findings of this study, whereas the complete set of experimental results is provided in Appendix A.

As the reflected pressure histories indicate the loading experienced by the target plates, they are presented in Section 4.1. It should be noted that a slightly different time axis is used for the presented pressure histories compared to the displacements, i.e., two different time axes are defined for the plotted results. For the pressure histories, $t = 0$ is set to the point in time where the incoming pressure passes Sensor 1 on its way towards the target plate. This is done to visualize both the incoming and reflected pressure as two separate peaks. For all deformation histories, $t = 0$ was set to the last measurement before any deformation occurred in the target plate. This allows for a better comparison of the dynamic response.

4.1. Plates without defects

Fig. 5 presents the pressure histories measured at Sensor 1 for the tests on D6 and D14 plates without any defects. Table 4 provides the nominal firing pressure, peak incoming pressure $P_{so,max}$ and peak reflected pressure $P_{r,max}$ for each test. It is emphasized that Sensor 1 is located 245 mm upstream the target plates (see Fig. 3) and that the initial rise in pressure corresponds to the incoming pressure wave, while the second peak is due to the reflected pressure wave on its way back towards the driver section after impacting the target plates. One important observation in Fig. 5 (a)–(b) is that similar firing pressures result in a similar pressure history for the incoming blast wave when varying the plate material. This confirms the repeatability of the
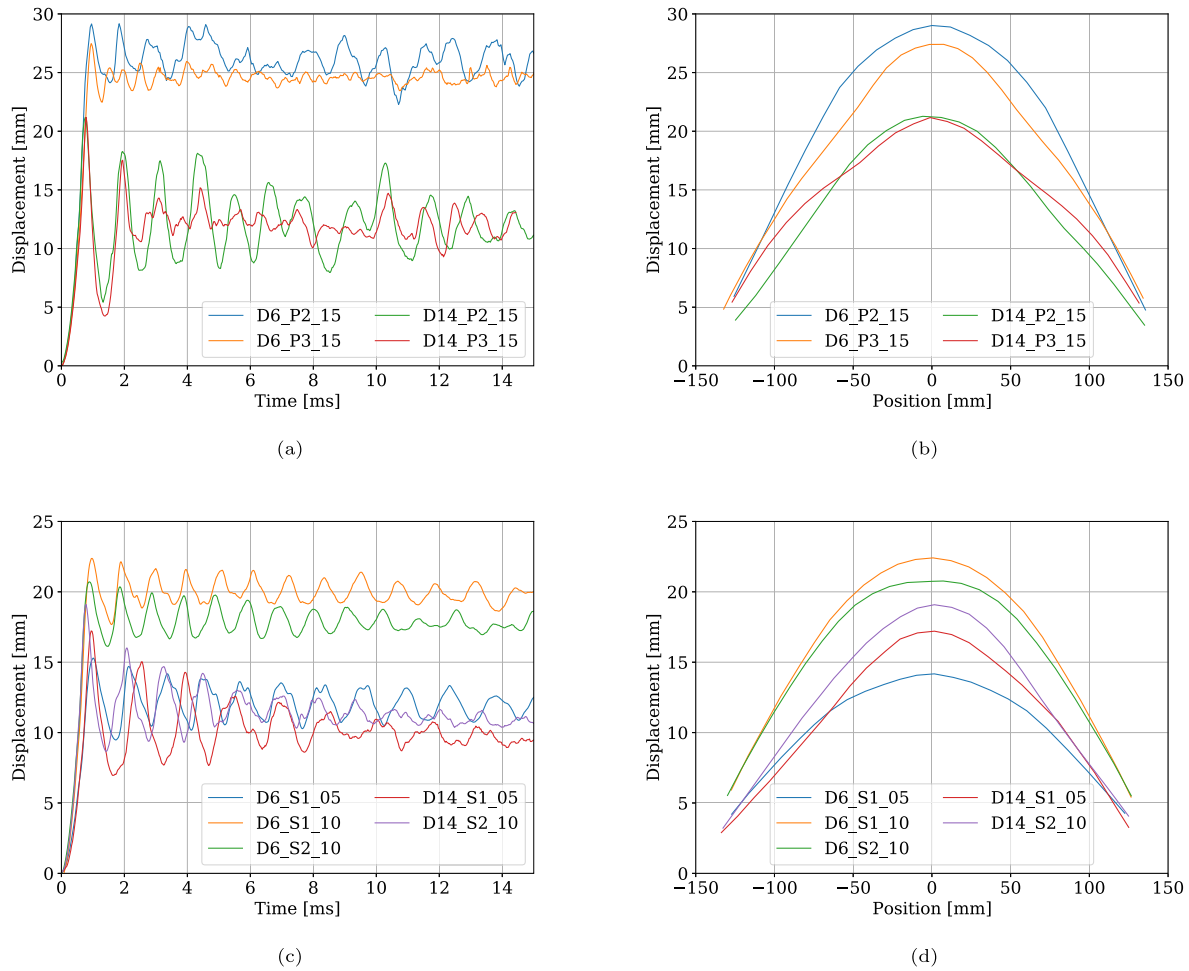
(a)

(b)

(c)

(d)

Fig. 8. Deflection measurements for tests on plates with pre-formed holes (P2 and P3), and pre-formed slits (S1 and S2) for both materials (D6 and D14): (a) and (c) show mid-point displacements histories, and (b) and (d) give the corresponding deformation profiles at $d_{z,max}$.

tests and enables detailed studies on various geometries and materials exposed to the same blast intensity. The peak reflected pressure at Sensor 1 is influenced by the dynamic response of the plate. This is also observed in Fig. 5 where slightly lower magnitudes of reflected pressure are observed for the D6 plates when exposed to the same blast intensity as the D14 plates. A plausible explanation for the different magnitudes of the reflected pressure is fluid–structure interaction (FSI) effects during the initial response of the plates, i.e., before the plates have obtained their permanent deflection (see e.g., [36]). However, these FSI effects are considered as beyond the scope of this study and detailed studies on FSI effects are suggested as future work. Pressure histories for the remaining tests are given in Appendix A.1.

The effect of changing the steel material from D6 to D14 on the global response of the plates is presented in terms of mid-point displacements in Fig. 6 (see also Table 4). When the blast wave impacts the target plate, an abrupt displacement is observed, followed by comparatively small oscillations. As expected, it is observed significantly larger displacements for the D6 plates when exposed to the same blast intensity as the D14 plates. It should be noted that similar colours in the figures represent the same blast intensity and that none of the plates without initial defects failed or ruptured during the tests.

Fig. 6 shows that the elastic oscillations are larger for the D14 plates than the D6 plates. For the D6 plates, the largest oscillations are found at the lowest blast intensity (D6_FP_05) and the magnitude of the elastic oscillations are reduced as the load intensity is increased.

The resistance against elastic oscillations is assumed to have two main contributors; first, the plastic dissipation of energy until the maximum displacement $d_{z,max}$ is reached, and second, the geometry of

Table 4
Experimental results from the full plate (FP) tests measured with 3D-DIC. The firing pressure is the last measured pressure in the driver before the sudden pressure drop at diaphragm rupture, $P_{so,max}$ and $P_{r,max}$ are the maximum incoming and maximum reflected pressure measured at Sensor 1, while Δd is calculated as $(d_{z,max} - d_{z,p})/d_{z,max}$.

Test	Firing pressure [bar]	$P_{so,max}$ [kPa]	$P_{r,max}$ [kPa]	$d_{z,max}$ [mm]	$d_{z,p}$ [mm]	Δd [%]
D6_FP_05	5.16	111.5	254.4	15.62	10.71	31.4
D14_FP_05	5.18	115.5	246.6	15.72	3.42	78.2
D6_FP_15	15.83	219.6	563.3	25.25	21.84	13.5
D14_FP_15	15.07	227.0	604.2	20.90	7.60	63.6
D6_FP_25	26.15	288.1	776.5	31.73	28.57	9.9
D14_FP_25	23.61	282.0	852.7	25.00	12.05	51.8
D6_FP_35	36.92	328.4	1038.8	36.07	34.43	4.5
D14_FP_35	36.18	348.5	1147.5	32.22	19.24	40.3
D6_FP_60	61.18	435.8	1372.0	45.10	43.70	3.1
D14_FP_60	61.91	455.3	1499.0	36.15	26.49	26.7

the permanent deformed configuration of the target plates at $d_{z,max}$. From Fig. 7, it is observed that the target plates deforms into a dome-shaped configuration, which adds a geometric stiffness against elastic springback. The magnitude and shape of the deformed configurations are further assumed to depend on both the strength and the work hardening of the plate material.

It is further noted that the D14 target plate exposed to the lowest blast intensity (D14_FP_05) undergoes negative displacements at about 40 ms in Fig. 6(b). Negative displacements are defined as displacements
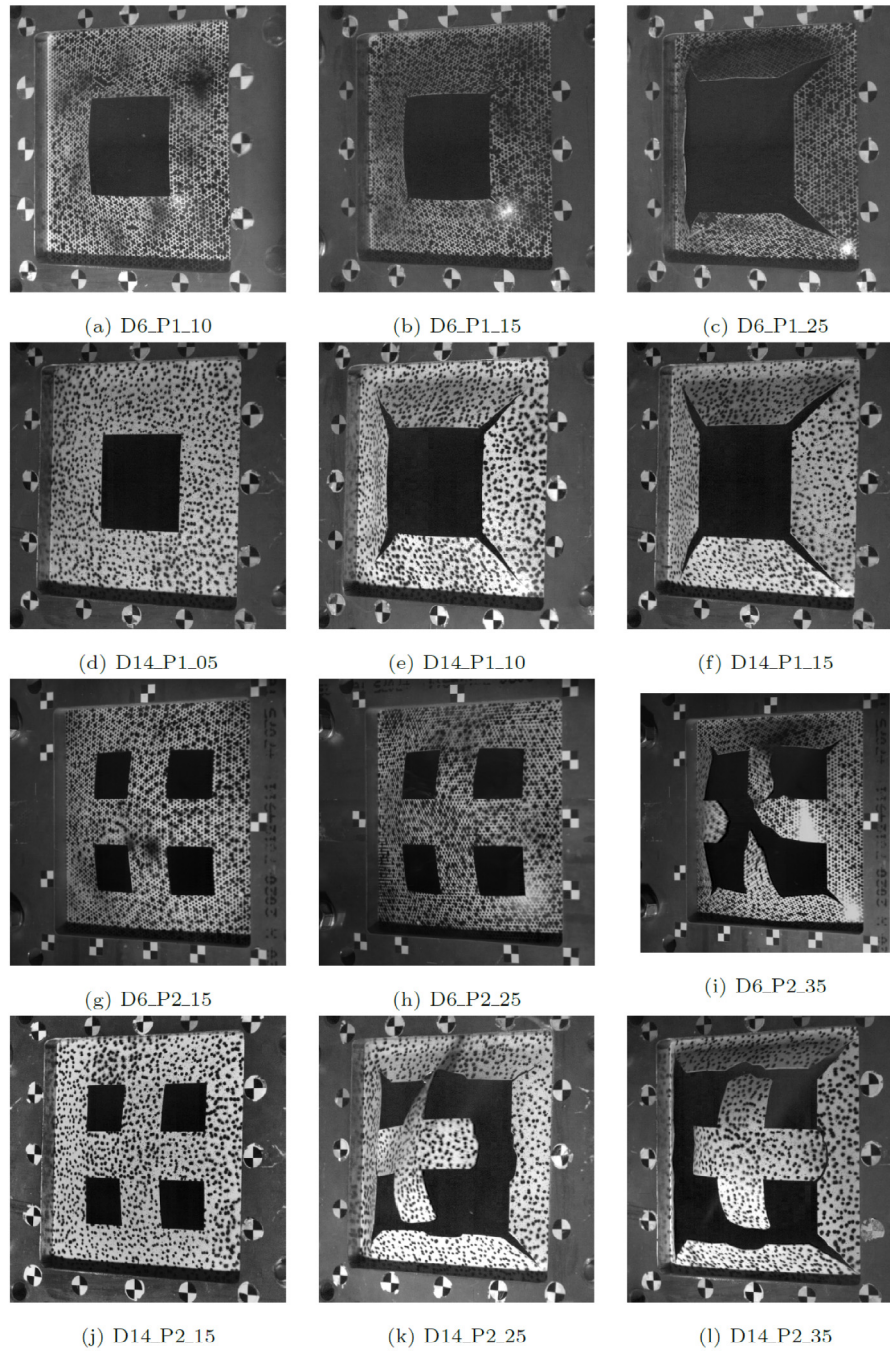
Fig. 9. Fracture modes for tests on plates with pre-formed holes (PX). The images are taken from one of the high-speed cameras and the test name is given in the sub-caption of each image.

in the opposite direction as the incoming blast wave, commonly known as counter-intuitive behaviour. By considering the corresponding pressure history in Fig. 5, it is observed that the negative displacements occur during the negative duration of the reflected pressure. This phenomenon was also discussed by Aune et al. in [22]. However, negative displacements only occurred for the D14 material. All experiments experiencing negative displacements are given in Appendix A.3.

A more detailed insight on the response of the plates is gained by assessing the shape of the target plates during deformation. Fig. 7 provides the deformation profiles measured by 3D-DIC. Deformation profiles for the D6 plates are given in Fig. 7(a)–(c) and the D14 plates are given in Fig. 7(d)–(f). These profiles represent the out-of-plane

displacements along a horizontal line across the entire blast exposed area (see the blue line in Fig. 3). To gain insight into the deformation history of each plate, the deformed state at maximum deflection $d_{z,max}$ (red line) and the minimum deflection $d_{z,min}$ after the first elastic springback (blue line) are shown. The movement from $d_{z,max}$ to the first minimum $d_{z,min}$ is denoted the initial elastic springback, which is illustrated in the subplot in Fig. 7(a). The green curves illustrate the plate movement during the initial elastic springback for intervals of 0.027 ms. It should be noted that the blast wave travels back and forth inside the shock tube several times until a static overpressure is reached when the air comes to rest. This leads to multiple loading events on the plate such that the final configuration may not be representative
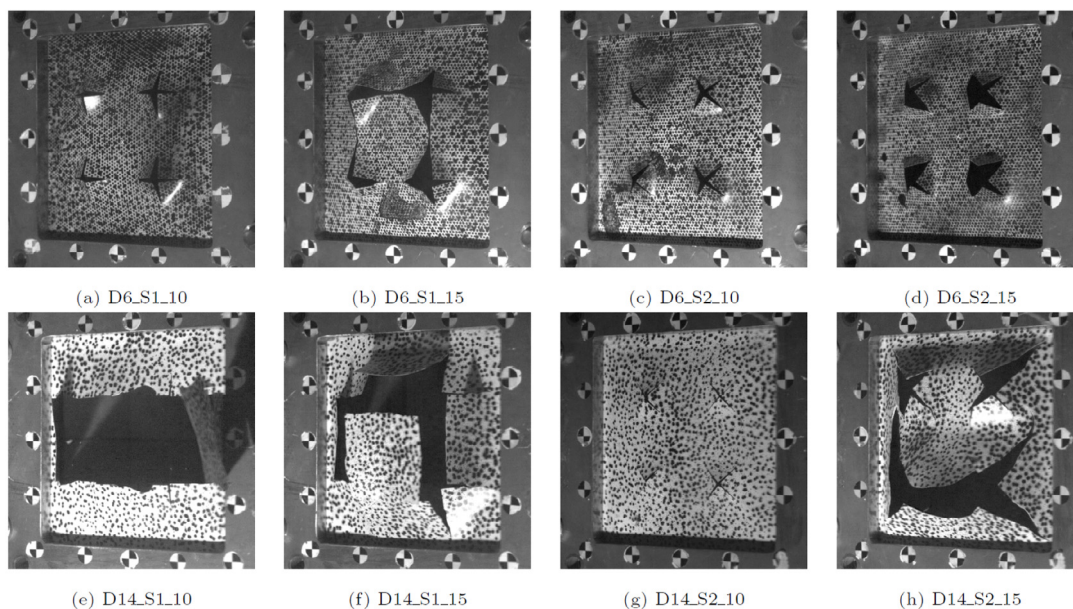
Fig. 10. Fracture modes for tests on plates with pre-formed slits (SX). The images are taken from one of the high-speed cameras and the test name is given in the sub-caption of each image.
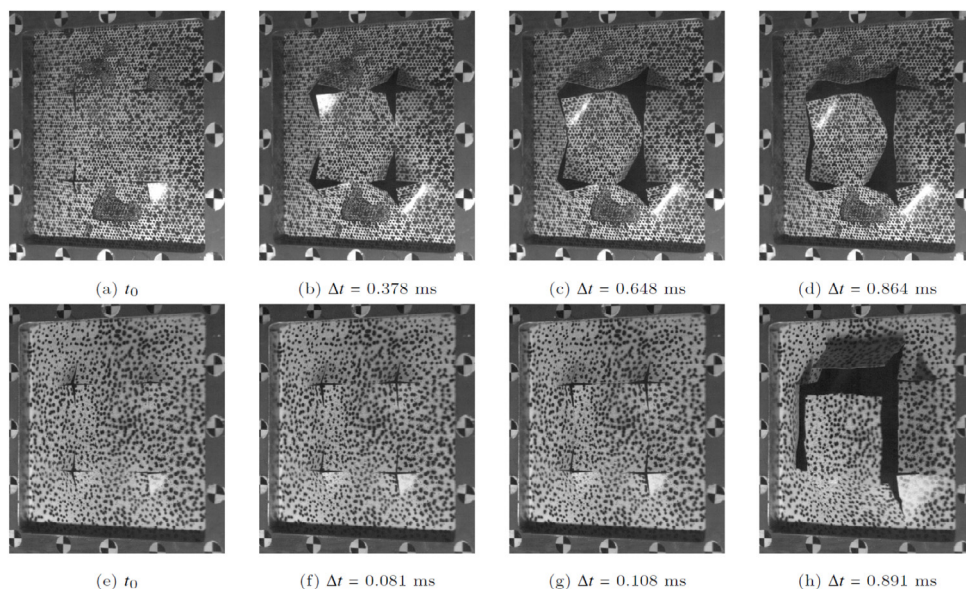

Fig. 11. Crack propagation for the S1 geometry at the highest blast intensity for test D6_S1_15 (top row) and test D14_S1_15 (bottom row). The images in the left column represent the instant before any visual cracks occurred, whereas the following images are presented for characteristic times during the fracture process.

for the primary loading event. It was therefore decided not to include the permanent deformation profile in Fig. 7.

Fig. 7 shows that the deformed shapes are different for the two plate materials, indicating different plastic strain distributions. As also observed by Aune et al. [20], the deformations initiate near the clamped area and propagate towards the centre of the plate, resulting in a parabolic shape at $d_{z,max}$. For the D6 plates, springback is observed only on a local part of the plate near its centre. In contrast, springback is observed along most of the plate width for the D14 plates for the same blast intensities.

The experimental results are compiled in Table 4, giving the maximum ($d_{z,max}$) and the permanent ($d_{z,p}$) mid-point deflection for all tests on the full plates. Table 4 also contains information on the amount of elastic deformations in the plates (Δd) which is calculated based on

the difference in $d_{z,max}$ and $d_{z,p}$. The maximum displacement ($d_{z,max}$) is taken as the maximum value during the test, while the permanent displacement ($d_{z,p}$) is estimated by finding the average value for the last 2.7 ms of the measured displacement history.

4.2. Plates with pre-formed defects

Due to the extensive number of experiments on plate geometries with pre-formed defects, displacement plots from only a representative selection of tests is provided in this section. Fig. 8 presents mid-point displacements and the corresponding deformation profiles at maximum deformation ($d_{z,max}$) for plates with pre-formed holes in (a)–(b), and slits in (c)–(d). The P1 and S3 geometries are not presented due to the absence of a midpoint (see Table 3). Similar as for the plates

Table 5
Displacement measurements obtained from 3D-DIC on the plates with pre-formed holes (PX) and slits (SX). Deformation measurements of tests experiencing complete fracture are given as (-), while geometries without a midpoint are denoted NA. The given firing pressure is the last measured pressure in the driver before the sudden pressure drop at diaphragm rupture.

Test	Firing pressure [bar]	$P_{so,max}$ [kPa]	$P_{r,max}$ [kPa]	$d_{z,max}$ [mm]	$d_{z,p}$ [mm]	Δd [mm]	Damage
D6_P1_05	5.17	107.0	228.3	NA	NA	NA	No cracks
D14_P1_05	5.16	103.9	226.6	NA	NA	NA	Crack arrest
D6_P2_05	6.18	110.2	225.9	18.29	13.77	4.27	No cracks
D14_P2_05	5.17	112.1	214.7	14.45	2.58	11.87	No cracks
D6_S1_05	5.19	109.8	240.0	15.29	11.42	3.87	No cracks
D14_S1_05	5.15	111.2	254.6	17.23	0	17.23	No cracks
D6_P1_10	10.12	173.6	384.7	NA	NA	NA	Crack arrest
D14_P1_10	9.93	166.4	377.3	NA	NA	NA	Complete fracture
D6_S1_10	10.03	168.2	413.4	22.38	19.16	3.22	Crack arrest
D6_S2_10	9.98	164.6	383.2	20.71	17.49	3.22	Crack arrest
D14_S1_10	10.07	161.6	406.7	–	–	–	Complete fracture
D14_S2_10	10.03	165.5	414.7	19.10	7.16	11.94	Crack arrest
D14_S3_10	10.07	165.7	410.3	NA	NA	NA	Complete fracture
D6_P1_15	15.42	224.0	510.3	NA	NA	NA	Crack arrest
D14_P1_15	15.13	222.8	535.6	NA	NA	NA	Complete fracture
D6_P2_15	16.38	219.2	491.2	29.91	26.35	3.55	Crack arrest
D14_P2_15	15.06	230.9	490.4	21.17	11.81	9.36	No cracks
D6_P3_15	15.65	225.8	495.7	27.43	24.19	3.33	Crack arrest
D14_P3_15	15.08	222.8	481.2	21.18	11.77	9.41	No cracks
D6_S1_15	15.61	213.7	543.5	–	–	–	Complete fracture
D6_S2_15	15.34	227.9	571.1	26.36	23.22	3.14	Crack arrest
D14_S1_15	15.10	216.8	552.1	–	–	–	Complete fracture
D14_S2_15	15.10	229.4	568.0	–	–	–	Complete fracture
D14_S3_15	15.08	229.1	574.2	NA	NA	NA	Complete fracture
D6_P1_25	24.45	281.5	661.7	NA	NA	NA	Complete fracture
D6_P2_25	26.98	300.9	709.0	35.67	33.18	2.48	Crack arrest
D14_P2_25	24.73	276.5	688.7	–	–	–	Complete fracture
D6_P3_25	24.62	280.8	663.5	38.16	34.27	3.89	Crack arrest
D14_P3_25	24.64	294.8	708.8	–	–	–	Complete fracture
D6_S2_25	25.14	290.8	744.8	37.15	31.59	5.56	Crack arrest
D14_S2_25	24.61	290.5	790.8	–	–	–	Complete fracture
D6_S3_25	24.55	281.3	745.2	NA	NA	NA	Crack arrest
D14_S3_25	24.57	279.9	728.9	NA	NA	NA	Complete fracture
D6_P2_35	37.68	357.7	883.5	–	–	–	Complete fracture
D14_P2_35	36.63	339.7	875.5	–	–	–	Complete fracture
D6_P3_35	38.11	353.9	871.4	–	–	–	Complete fracture
D14_P3_35	37.68	–	–	–	–	–	Complete fracture
D6_S3_35	37.32	358.0	1033.6	NA	NA	NA	Complete fracture

without defects, the pressure measurements and displacement data for the experiments are represented in Table 5. The results are organized in the same way as for those of the plates without defects in Table 4. The displacement histories not included in this section are given in Appendix A.2.

When introducing defects to the target plates, the clear trend was a shift from large plastic deformations (without any signs of crack initiation) to crack initiation and crack propagation. For target plates with defects, the effects of changing the steel material from D6 to D14 on the global response follow the same trends as for the full plates. As long as the plates do not fail, the D14 plates experience less deformation and more pronounced oscillations around the permanent deformed configuration (see Fig. 8). As for the plates without pre-formed defects, the peak reflected pressure was observed to be slightly reduced for the D6 plates relative to the D14 plates (see Table 5).

The effect of changing the plate geometry on the global response of the plates is represented using two geometries with pre-formed holes (P2 and P3) and two geometries with slits (S1 and S2), shown for the two lowest blast intensities in Fig. 8. The plates presented in Fig. 8 did not experience any visible fracture during the tests. From the overall global response in Fig. 8, it is seen that the plate material influence the response more than the plate geometry. That is, the D6 plates undergo the largest displacements for all geometries, and the D14 plates give the largest oscillations for all geometries. Moreover, the comparison of

the deformation profiles in Fig. 8(d) indicates that the plate material also has an influence on the deformed shape of the plates. The D14 plates have a more pointed deformed shape than the D6 plates, which is interesting in view of the different work hardening characteristics (see Fig. 1).

4.3. Fracture modes and crack propagation

In short, the plates without fracture behaved according to the initial expectations of this study. That is, higher strength leads to increased blast resistance of the plates resulting in smaller magnitudes of deformation. However, in contrast to the plates without defects, most of the plates containing initial defects experienced crack initiation and crack propagation. Despite its higher material strength, the D14 plates consistently fractured at lower blast intensities than the D6 plates. Another observation was that the tests on D6 plates covered three distinct responses depending in the blast intensity. That is, the lowest blast intensity resulted in small plastic deformations without any crack initiation, while increasing blast intensities resulted in larger plastic deformations and arrested cracks at the intermediate intensities until complete fracture was observed for the highest load intensities. This was more or less as expected. However, it was interesting to note that these three different responses were not as evident for the D14 plates, where the plates mainly experienced either plastic deformations
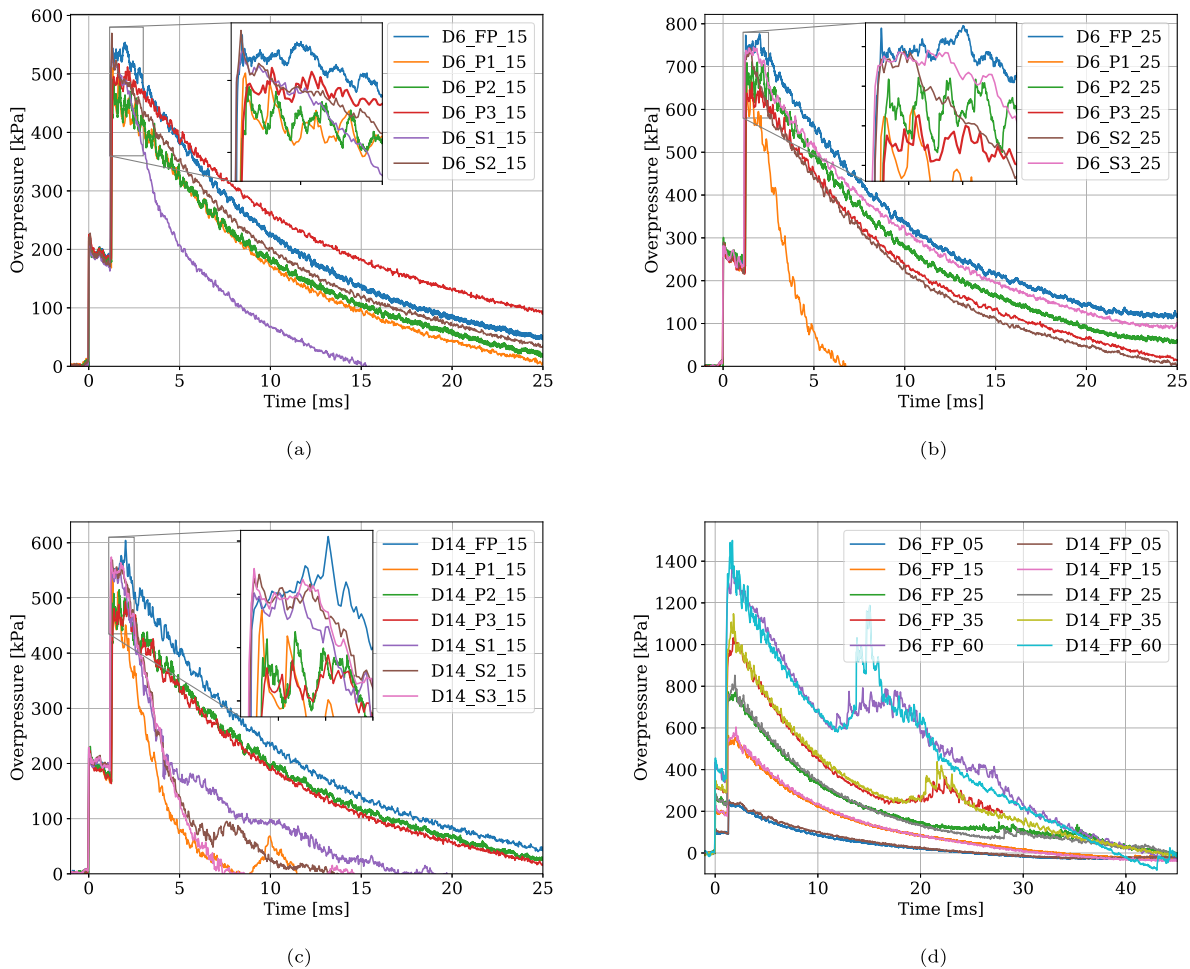
Fig. A.1. Pressure–time histories for the tests on the D6 and D14 plates, comparing perforated plates (holes vs slits) to the full plate configuration. A zoomed plot is also provided around the peak reflected pressure to enable a better comparison of the configurations.

without any cracking or complete fracture. The only exception was test D14_P1_05 which resulted in arrested cracks.

As expected, the geometry of the pre-formed defects was also found to have a pronounced influence on the blast resistance of the plates. By comparing the damage characteristics of the plates with holes and slits presented in Table 5, it is evident that complete fracture is more frequently observed in geometries with slit defects than plates with holes. For plates with pre-formed holes (PX), 7 out of the 21 tests resulted in crack arrest while 9 of the tests resulted in complete fracture. Similarly, for plates with slits (SX), crack arrest was found in 6 out of the 16 tests while 8 tests resulted in complete fracture.

Figs. 9 and 10 present images of the target plates captured by one of the high-speed cameras during testing, showing the fracture modes for a representative selection of tests on plates with pre-formed holes (PX) and pre-formed slits (SX), respectively. The presentation is further limited to tests experiencing either partial or complete fracture. For completeness, the fracture modes of the remaining experiments are presented in Appendix B.1.

The P1 geometry showed the lowest capacity to fracture and resulted in the same fracture mode for both materials. For the P2 geometry, the effect of changing the plate material caused a shift in fracture mode. Two distinct fracture modes were observed, where the fracture mode seemed to be determined by the plate material. The D6 plates experienced cracks propagating along the diagonals until the

plate reached complete fracture (see test D6_P2_35 in Fig. 9), whereas the D14 plates fractured along the horizontal and vertical extremities in-between the holes resulting in a cross-shaped fracture mode (see tests D14_P2_25 and D14_P2_35 in Fig. 9). It should be noted that only one of the tests resulted in complete fracture for the P2 geometry in the tests with D6 plates (D6_P2_35), which makes it challenging to draw any general conclusions for this particular geometry. However, assessing all the tests on plates with pre-formed holes, it is evident that the fracture mode and crack propagation are influenced by the material of the plates. It is interesting to note that the D6 plates seem to outperform the D14 plates under similar load intensities, given the fact that the D14 material has significantly higher strength than the D6 material (see Fig. 1).

Fig. 10 provides the same presentation of the fracture modes for tests on plates with pre-formed slits (SX). As for the geometries with pre-formed holes, a representative selection of the tests are presented (i.e., S1 and S2 geometries). The clear trend was that the plates with slit geometries (SX) fractured at lower load intensities than the plates with pre-formed holes (PX). The cracks always initiate at the extremities of the slits and started to propagate in the slit direction until the cracks reached the supports or reaches the path of other cracks. In contrast to the plates with pre-formed holes, the plate material were not observed to influence the fracture mode of the plates. This is clearly illustrated in
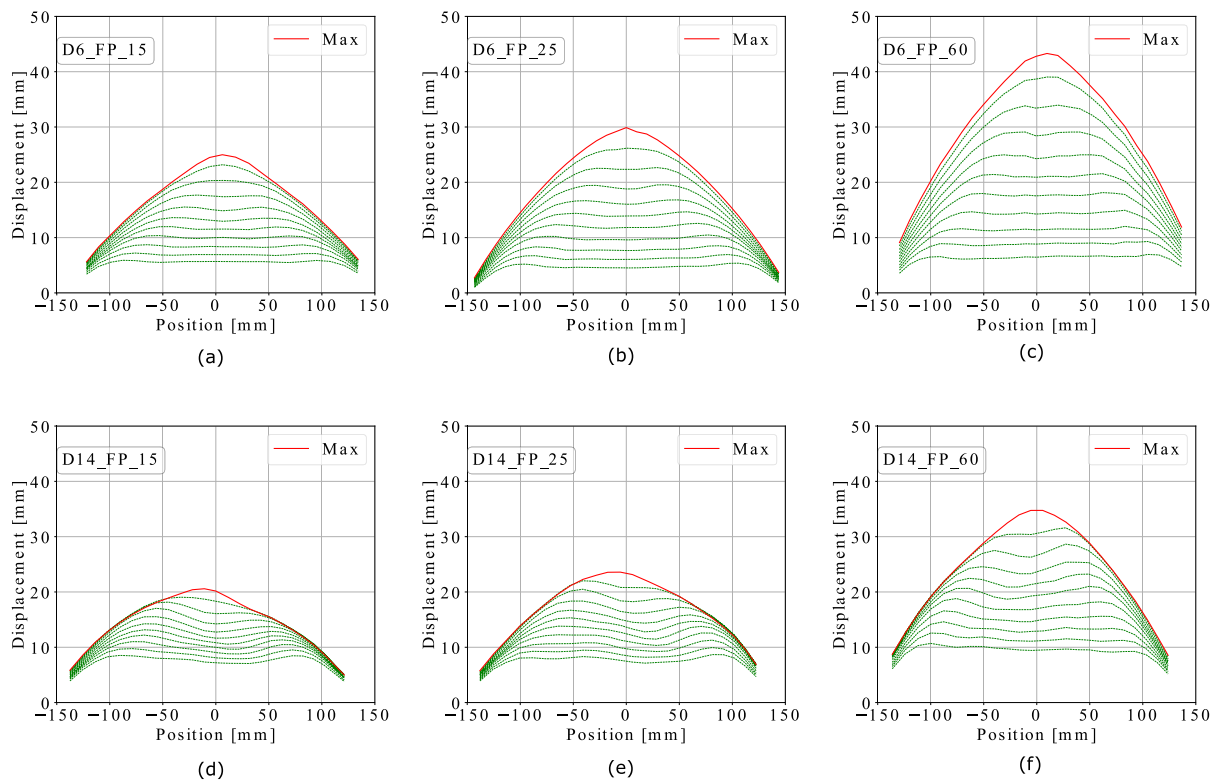
Fig. A.2. Development of deformation profiles until maximum deflection for the FP configuration, exposed to a blast intensities corresponding to firing pressures of 15, 25 and 60 bar. A selection of the D6 plates are shown in (a)–(c) and a similar selection of D14 plates in (d)–(e). The red line indicates the maximum displacement, whereas the green lines show the development in time. The time difference between each green line is constant and equal to the sampling rate ($\Delta t = 0.027$ ms) between each green profile. (For interpretation of the references to colour in this figure legend, the reader is referred to the web version of this article.)

Fig. 11, showing the fracture process of the S1 plates in tests D6_S1_15 and D14_S1_15.

By considering the time it takes a crack to propagate from the extremities of the defects towards the supports of the plate, a significant difference in crack propagation velocity was observed between the two materials. Since both materials experienced identical crack propagation paths to complete fracture for identical blast intensities for the S1 geometry presented in Fig. 11, it was decided to measure and compare the velocities of the propagating cracks from these tests. By visual evaluation of the high speed image recordings, the mean crack propagation velocity was found to be in the range 60–75 m/s and 220–280 m/s for D6 and D14, respectively. This builds confidence in that there is a strength–ductility trade-off in the blast performance of the plates, because the D6 plates outperform the D14 plates in both blast resistance and a larger ability to arrest cracks before the plates reach complete fracture.

5. Discussion

For target plates not experiencing fracture, the findings in this study are well aligned with previous studies on both full plates and plates with pre-formed defects, see e.g., [20,29]. That is, an increase in material strength resulted in smaller displacements and larger elastic oscillations for a given blast intensity. Larger deformations for the low strength material are justified by the significantly lower yield stress, causing larger plastic deformations for a given load intensity [29]. As the strongest material (D14) has a significantly higher yield stress, this material will experience much higher internal stresses at maximum deformation. The increased internal stress state will in turn lead to

higher internal forces for the elastic rebound, possibly causing larger oscillations. It is important to keep in mind that all blast tests on plates without any pre-formed defects resulted in global deformation without any signs of fracture. However, as pre-formed defects were introduced, the trend in global response remained unchanged, but fracture occurred for the highest load intensities.

The observations in this study indicate that the blast resistance is higher in the most ductile material despite its reduced strength. The strongest material (D14) was more prone to fracture and consistently fractured at lower blast intensities than the more ductile material (D6). High strength is typically accompanied by low ductility [27] and it is therefore not guaranteed that higher material strength leads to increased blast resistance of perforated steel plates. Ductile fracture is generally governed by local plastic deformation in a material [37], and the distribution of plastic strain tends to depend on the work hardening of the plate material during blast loading (see e.g., Ref. [29]). That is, a material with limited work hardening will experience a more distinct localization of plastic deformation, and hence, a more rapid increase of plastic strains within the localized areas. It is emphasized that it is very challenging to quantify the effect of work hardening on the blast resistance of thin steel plates based on the experiments presented in this study, and further work involving numerical simulations is required for a more detailed investigation of the topic.

The D6 plates generally resulted in three distinct fracture modes. First, plastic deformations without any signs of fracture, then larger plastic deformations and arrested cracks, before significant cracks or complete fracture were observed for the highest blast intensities. The fracture mode involving crack arrest was not that evident in the tests with the high-strength plates, where the cracks were arrested in only a
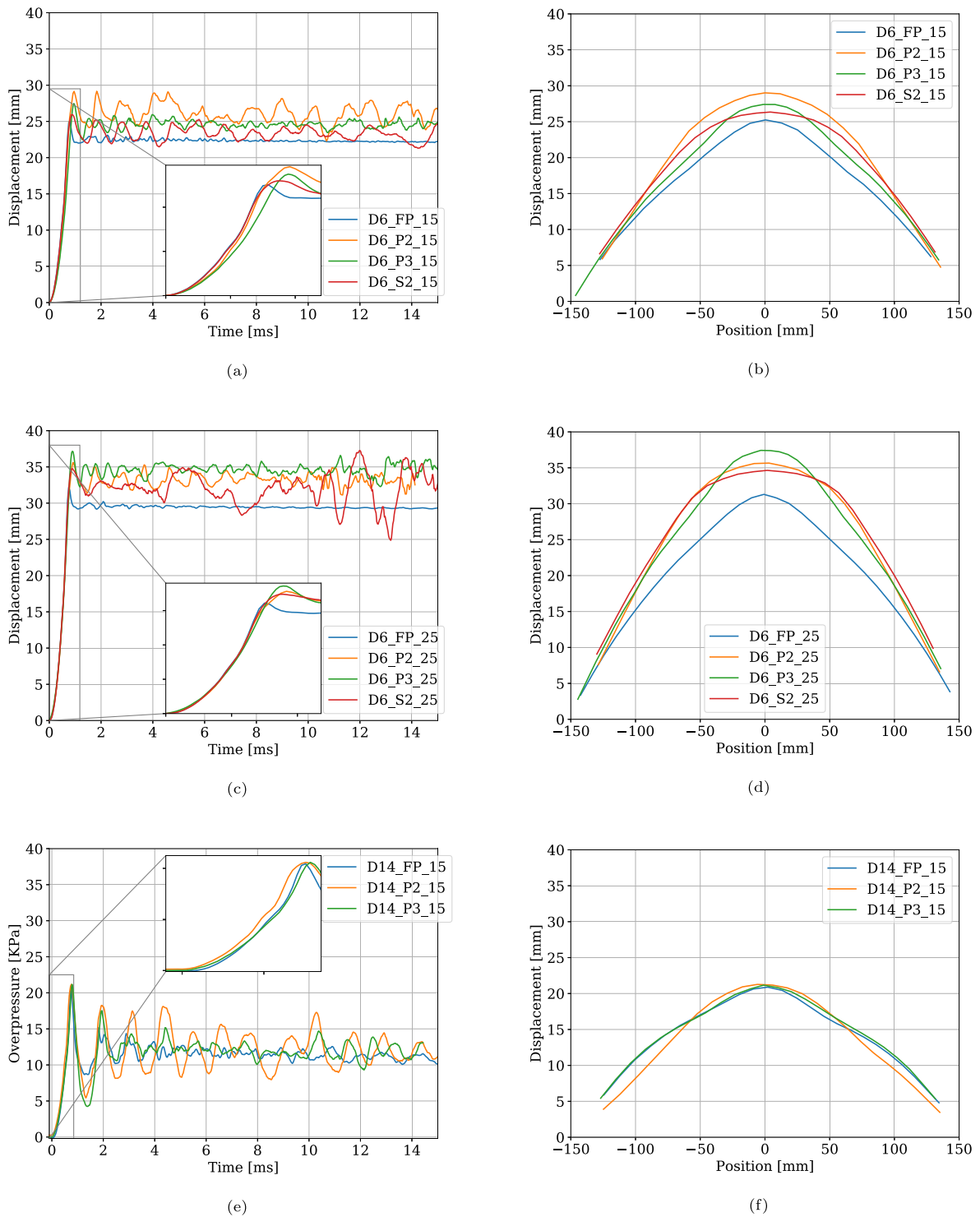
Fig. A.3. Mid-point displacements and deformation profiles at maximum displacement for tests on perforated plates (P2, P3, and S2) compared to the full-plate (FP) results at similar loading intensities (15 bar and 25 bar).

few tests for the D14 plates. That is, the D14 plates experienced either small plastic deformations without crack initiation or complete fracture as the blast intensity was increased. It is therefore reasonable to assume that the ability to arrest a propagating crack is strongly dependent

upon the ductility, which in turn governs the amount of energy dissipated during crack propagation. This assumption is supported by the observation that the more ductile material (D6) showed larger plastic deformations around the propagating cracks than the high-strength material (see Fig. 11). Thus, the tests on the D14 plates clearly showed
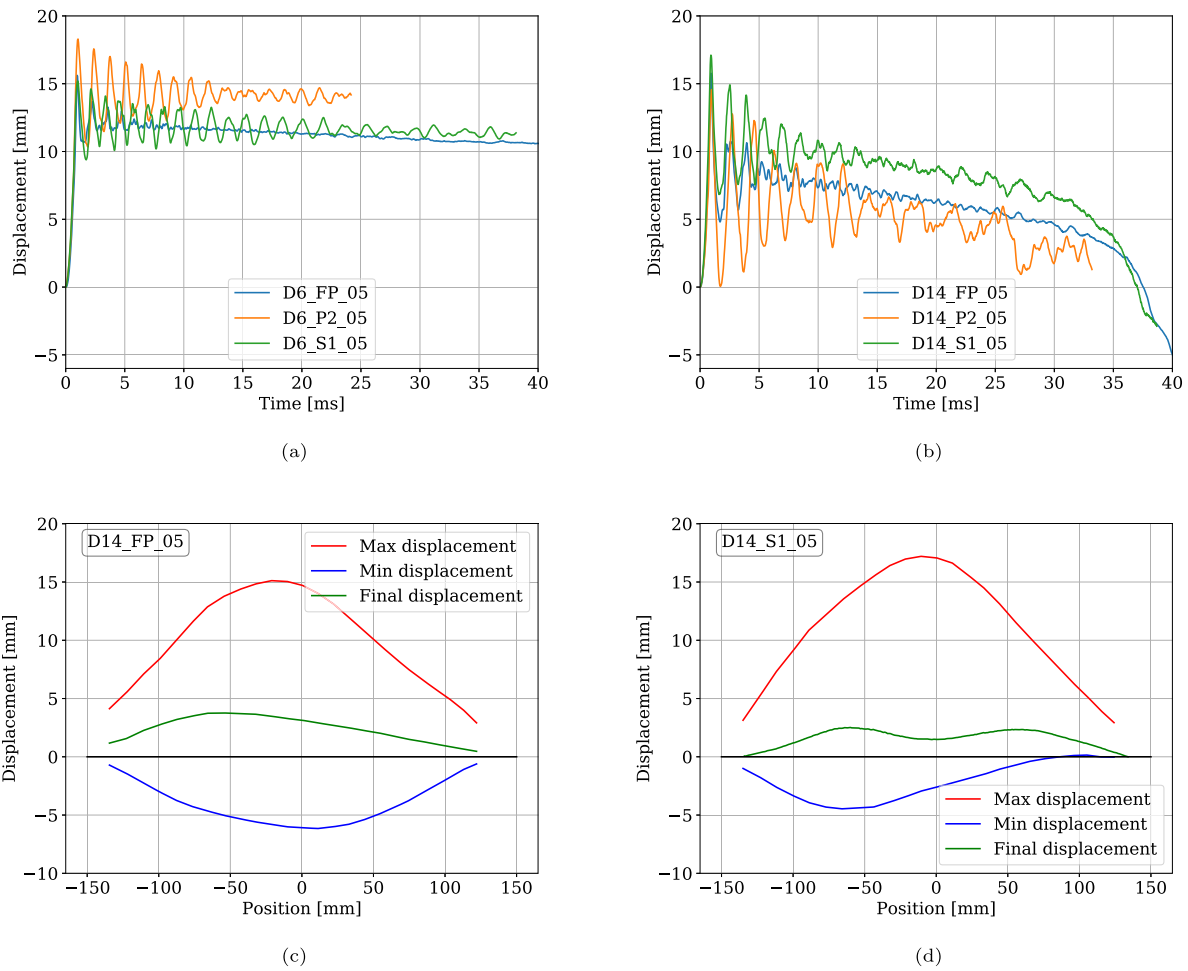
(a)

(b)

(c)

(d)

Fig. A.4. The mid-point displacements for all experiments exposed to blast intensities corresponding to a firing pressure of 5 bar are presented. The D6 target plates are presented in (a) and D14 plates in (b). The instants corresponding to the largest positive and negative displacement as well as the permanent displacement are shown for the D14_FP_05 and D14_S1_05 tests in (c) and (d), respectively.

Table B.1

Crack measurements for all tests that did not experience complete fracture. Measurements are made with reference to the crack identification introduced in Fig. B.3. Tests were only necking was observed is denoted with an N, while cracks that was too large to be practically measured have been identified by an X.

Test	O1	O2	O3	O4	I1	I2	I3	I4
D6_P2_05	–	–	–	–	–	–	–	–
D6_P2_15	N	N	N	N	N	N	N	N
D6_P2_25	7.41	8.35	8.68	7.83	11.76	13.56	15.67	12.62
D14_P2_05	–	–	–	–	–	–	–	–
D14_P2_15	N	N	N	N	N	N	N	N
D6_P3_15	N	N	N	N	N	N	N	N
D6_P3_25	N	N	N	N	2.0	2.4	1.6	2.2
D14_P3_15	N	N	N	N	N	N	N	N
D6_S2_10	N	N	N	N	4.4	4.7	4.3	4.2
D6_S2_15	5.1	4.4	4.7	4.8	11.4	10.8	10.9	10.3
D6_S2_25	22.8	22.2	21.2	22.5	X	X	X	X
D14_S2_10	N	N	N	N	N	1.6	N	2.0
	H1	H2	H3	H4	V1	V2	V3	V4
D6_S1_05	N	N	N	N	N	N	N	N
D6_S1_10	5.1	5.4	6.2	5.8	7.2	7.9	7.5	7.4
D14_S1_05	N	N	N	N	N	N	N	N
	O1	O2	O3	O4				
D6_P1_05	N	N	N	N				
D6_P1_10	6.1	6.2	6.4	6.1				
D6_P1_15	25.0	26.0	22.7	22.3				
D14_P1_05	5.99	9.96	17.14	4.24				

that cracks were allowed to propagate without any visual increase in global plastic deformations. In contrast to the findings in Ref. [29], the material did not only affect the capacity to fracture, but also the crack paths for experiments on the P2 geometry.

McDonald et al. [26] found that a high hardness armour steel with low ductility outperform a rolled homogeneous armour steel with higher ductility in terms of rupture threshold during blast loading. However, the target plates used in Ref. [26] were subjected to a different loading scenario, with a more localized and non-uniform loading on thicker target plates than those applied in the present study. In other words, the importance of the strength–ductility trade-off in the design of blast-resistant structures is expected to depend on both the loading conditions and the structural properties (i.e., the plate geometry and the material properties).

Finally, this study is motivated by more detailed studies into the influence of the strength–ductility trade-off on the performance of thin plates exposed to the combined effect of blast loading and fragment impacts. This topic was approached using a controlled laboratory environment and thin steel plates with pre-formed defects represented by square holes and cross-shaped slits. In realistic structures, pre-formed defects may also be present as e.g., bolt holes and window sections in facade elements, in addition to fragment or ballistic impact. Defects as a consequence of structural impact prior to the blast load would typically contain randomly distributed perforations with sharp notches and most likely accompanied with accumulated damage in front of the crack tip. Compared to the pre-formed defects investigated in this study, the additional ingredient of structural impact prior to the blast
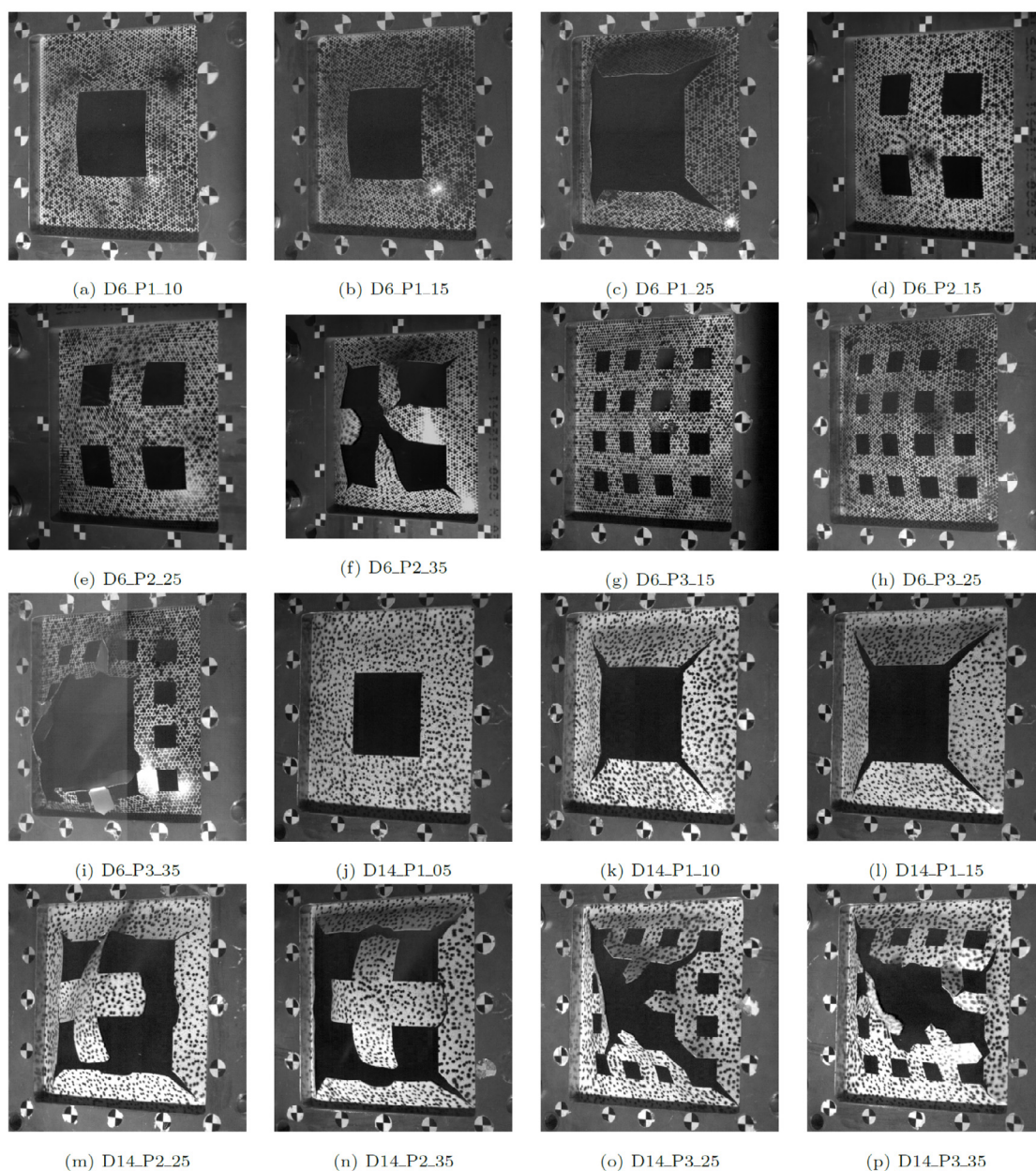
Fig. B.1. Fracture modes for tests on plates with pre-formed holes (PX). The images are taken from one of the high-speed cameras and the test name is given in the sub-caption for each image.

load is assumed to further reduce the capacity of the target plates. More realistic defects will also most probably result in less regularity in the observed fracture modes. Thus, the results in this study are not directly transferable to realistic design scenarios of combined fragment impact and blast loading. Similar studies should therefore be carried out on target plates with more complex initial defects and initial damage, aiding the design of future protective structures. However, such studies are considered beyond the scope of this study.

6. Concluding remarks

This work presents an experimental study on the influence of the strength–ductility trade-off on the blast resistance of thin steel plates

with and without pre-formed defects. The dynamic response of the plates showed a strong dependence on both the material properties (strength, work hardening and ductility) and the plate geometry (shape, number and spatial distribution of the pre-formed defects). The main findings of this study can be summarized as follows:

- In the absence of initial defects, the strength of the material was the primary property influencing the response of the plates. As expected, the target plates with higher strength resulted in smaller global deformations and larger elastic oscillations during blast loading. None of the plates without pre-formed defects showed any signs of crack initiation under the blast intensities applied in this study.
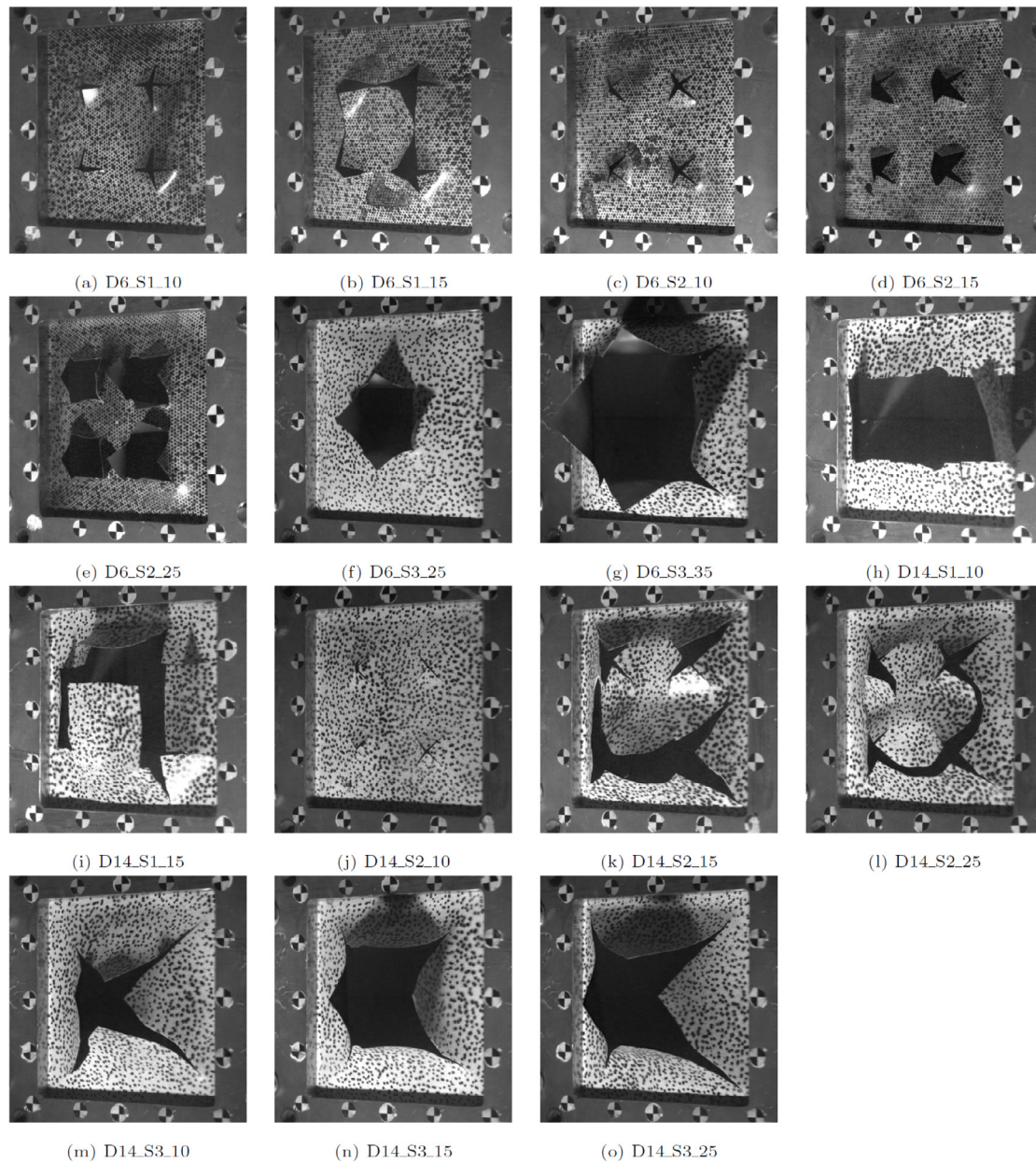
Fig. B.2. Fracture modes for tests on plates with pre-formed slits (SX). The images are taken from one of the high-speed cameras and the test name is given in the sub-caption for each image.

- When defects were introduced in the form of pre-formed holes, the high-strength (D14) plates consistently fractured at lower blast intensities than the medium-strength (D6) plates for identical plate geometries. This finding clearly shows that plates with higher strength are more prone to cracking and fracture than the plates with lower strength. As a higher strength typically is accompanied with a lower ductility, the results indicate that work hardening and ductility are more important than the strength for the capacity of pre-damaged and blast-loaded thin steel plates. However, for very sharp defects represented by pre-formed slits, both the medium- and high-strength materials resulted in the same fracture mode at similar blast intensities. Still, even though

less differences were observed in the fracture mode, the medium-strength (D6) plates outperformed the high-strength (D14) plates also for the tests on plates with pre-formed slits. This builds confidence in that there is a strength–ductility trade-off in the blast resistance of thin steel plates exposed to the combined effect of fragment impact and blast loading.

- The comprehensive experimental dataset presented in this study allows for validation and development of computational methods in future studies. This study also motivates further studies on the influence of the strength–ductility trade-off in protective design of combined fragment impact and blast loading scenarios.
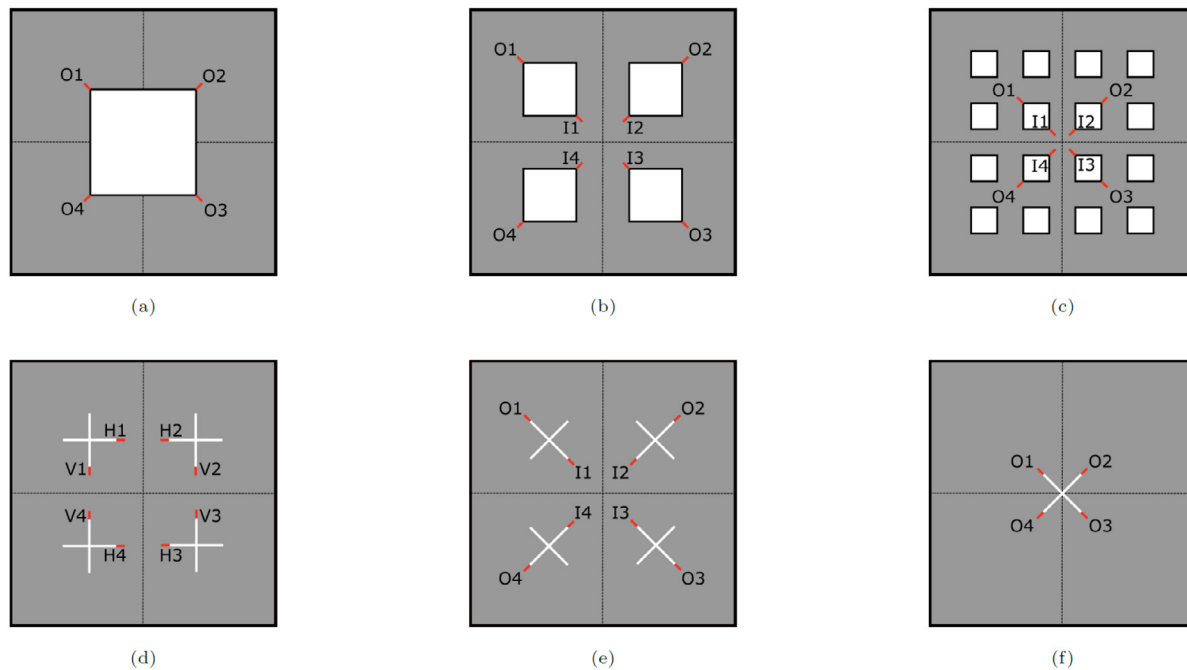
Fig. B.3. Location and naming conventions for measurements of arrested cracks for the selected tests. The cracks are indicated with red colour. (For interpretation of the references to colour in this figure legend, the reader is referred to the web version of this article.)
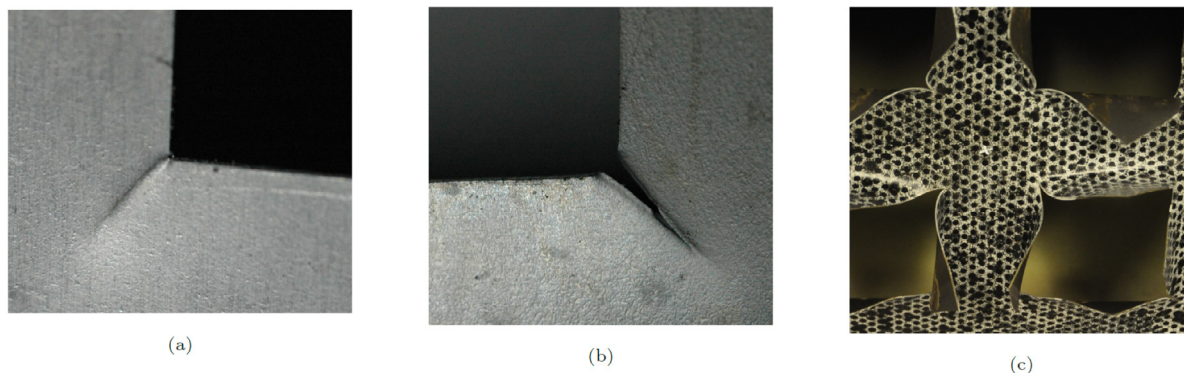

Fig. B.4. Images for some of the different fracture modes listed in Table B.1, where (a) shows a local necking (N) at the (O3) location for the D14_P2_15 experiment, (b) shows a crack at the location O4 for D6_P2_25 and (c) illustrates cracks in areas with plastic deformations too large to practically measure for D6_S2_25.

CRediT authorship contribution statement

Benjamin S. Elveli: Conceptualization, Data curation, Formal analysis, Visualization, Writing – original draft. **Mads B. Iddberg:** Conceptualization, Data curation, Formal analysis, Writing – review & editing. **Tore Børvik:** Conceptualization, Writing – review & editing. **Vegard Aune:** Conceptualization, Formal analysis, Writing – original draft, Funding acquisition, Supervision.

Declaration of competing interest

The authors declare that they have no known competing financial interests or personal relationships that could have appeared to influence the work reported in this paper.
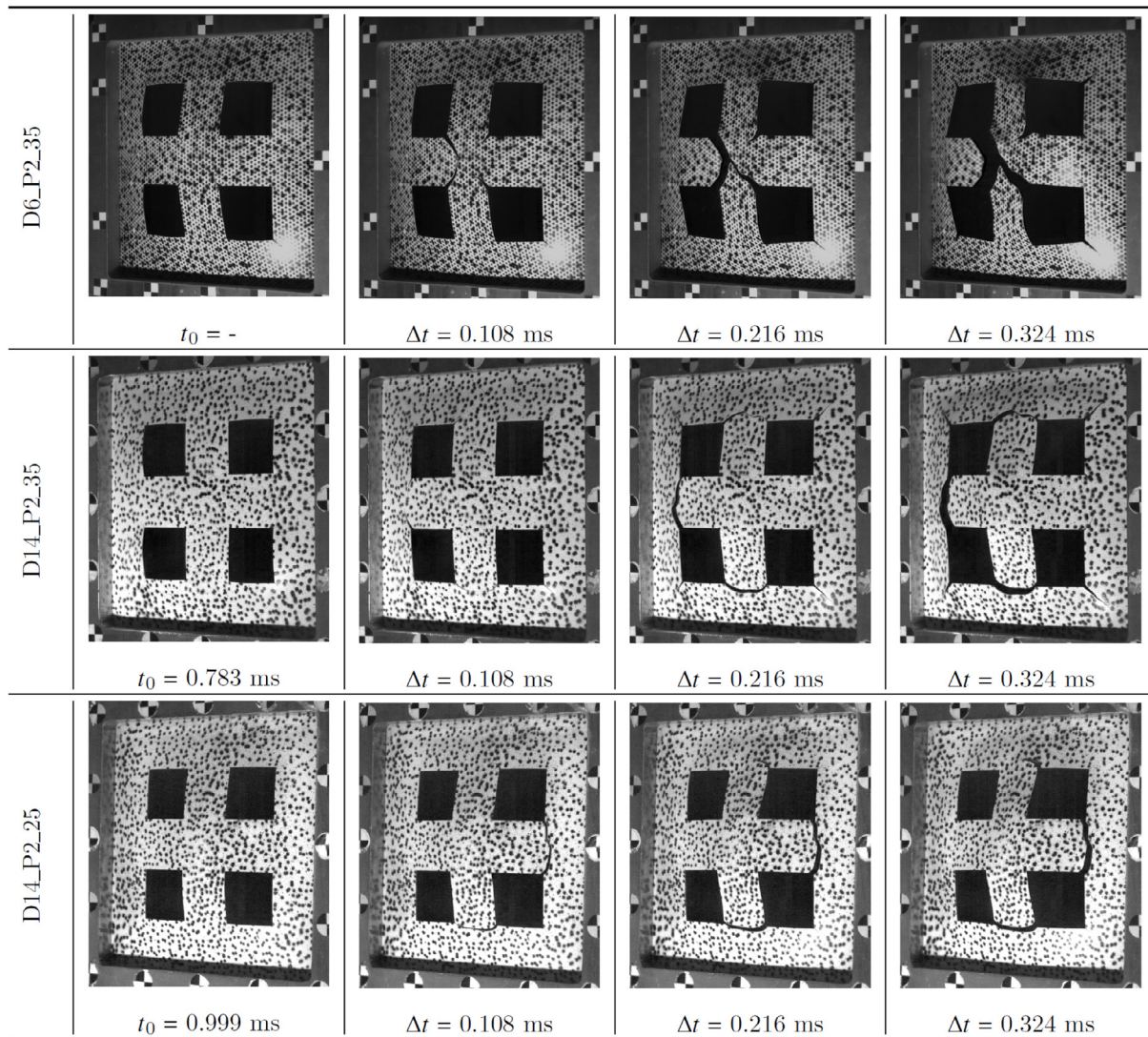
Fig. B.5. Images of the crack propagation for the P2 configuration exposed to blast intensities corresponding to firing pressures of 35 bar and 25 bar. Material, firing pressure and time for each image are given in the subcaptions. The given time for the images refers to the same time axis as the pressure plots, i.e., $t_0 = 0$ is defined as when the blast wave is passing the sensor closest to the target plate.

Appendix A

A.1. Global response - Pressure histories

Supplementary plots of the pressure histories measured at Sensor 1. In Fig. A.1, pressure curves are compared across the different geometries for a given material and pressure load in (a), (b) and (c). In (d) the pressure histories are compared for the two materials for the full plates (FP).

A.2. Global response - deformation histories

Fig. A.2 provides the development of the deformation profiles up to the instant of maximum deflection for the FP configuration. The upper and lower row presents results for the tests on D6 and D14 plates, respectively, when exposed to a blast intensities corresponding to nominal firing pressures of 15, 25 and 60 bar. The deformation profiles marked with red lines indicate the maximum displacement, whereas the green lines indicate the development of the deformations. Each green line corresponds to an image pair taken with the high-speed cameras. The time difference between each green line is constant and equal to the sampling rate ($\Delta t = 0.027$ ms).

The mid-point displacement histories for the perforated geometries (holes vs slits) are compared to the full plates (FP) in Fig. A.3. Note that these plots are the same tests as for the pressure histories given in Fig. A.1. The displacement histories in Fig. A.3 are presented with
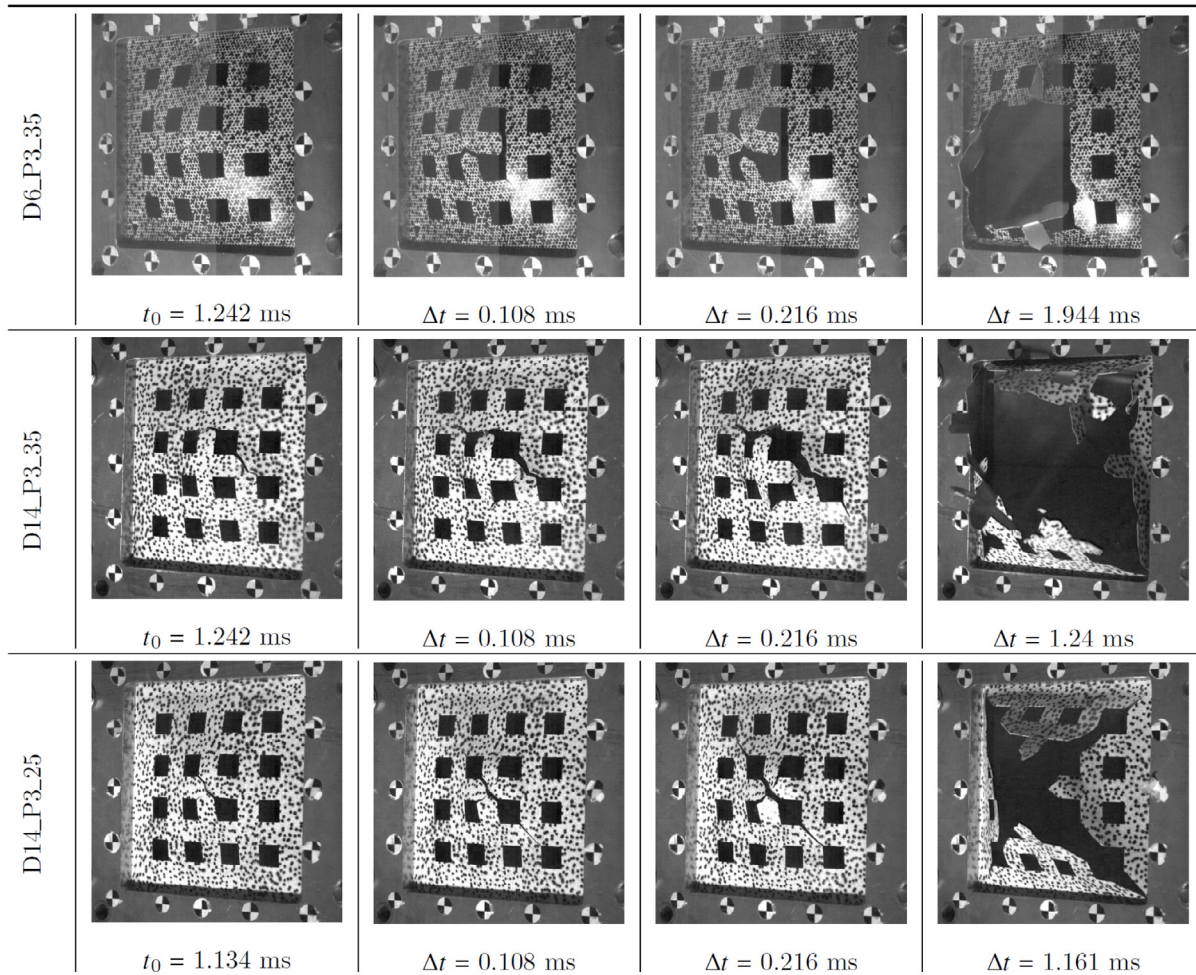
Fig. B.6. Images of the crack propagation for the P3 configuration exposed to blast intensities corresponding to firing pressures of 35 bar and 25 bar. Material, firing pressure and time for each image are given in the subcaptions. The given time for the images refers to the same time axis as the pressure plots, i.e., $t_0 = 0$ is defined as when the blast wave is passing the sensor closest to the target plate.

mid-point displacements in (a), (c) and (e), while the corresponding deformation profiles at the instant of maximum displacement is provided in (b), (d) and (f).

A.3. Counter-intuitive behaviour

As mentioned in Section 4.1, the D14 target plates experienced negative displacements for the test involving the lowest blast intensities. Negative displacements are defined as displacements in the opposite direction as the incoming blast wave, commonly known as counter-intuitive behaviour (CIB) (see e.g., Ref. [22]). Fig. A.4 shows a comparison of mid-point displacements for all experiments exposed to the lowest blast intensities for D6 plates in (a) and D14 plates in (b). In (c) and (d) the deformation profiles of two representative D14 tests are given for the maximum positive displacement, maximum negative displacement, and the permanent deflection.

Appendix B

B.1. Fracture modes

As only a selection of representative fracture modes were presented in Section 4.3, Figs. B.1 and B.2 show pictures of all tests experiencing either partial of complete fracture.

B.2. Crack initiation and crack arrest

The crack lengths for were used to investigate the influence of different materials and geometries on the resistance against localization and crack propagation. It was decided to measure the crack lengths for tests were this was possible from a practical point of view. The length of all visible cracks is for the tests under consideration is presented in Table B.1, where the locations and naming conventions of the cracks are defined in Fig. B.3. Localized necking without any visual cracking was denoted (N), whereas large cracks in areas with deformations too large to practically measure the cracks were denoted (X). All cracks were measured manually using a digital calliper. Images of cases experiencing necking (N), cracks, or cracks too large to measure (X) are given in Fig. B.4.

B.3. Crack propagation

Figs. B.5–B.8 provide image sequences of additional crack propagation to what was presented in Section 4.3. Each test corresponds to one row in each figure, where the image series and time evolution for each test are given in the columns.
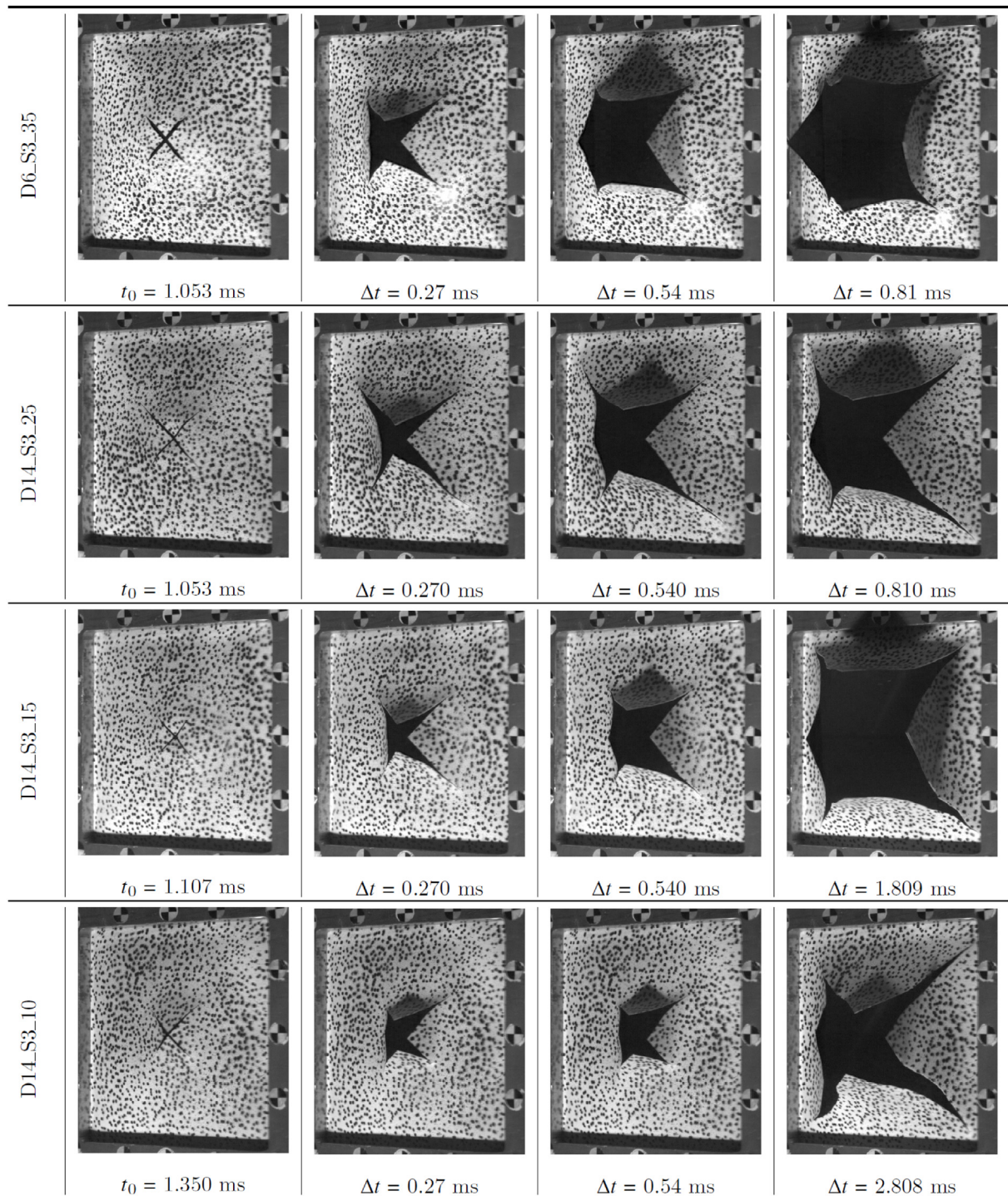
Fig. B.7. Image series of the crack propagation to complete fracture for the S3 configuration exposed to blast intensities corresponding to firing pressures of 35, 25, 15, and 10 bar, for both materials. The given time for the images refers to the same time axis as the pressure plots, i.e., $t_0 = 0$ is defined as when the blast wave is passing the sensor closest to the target plate.
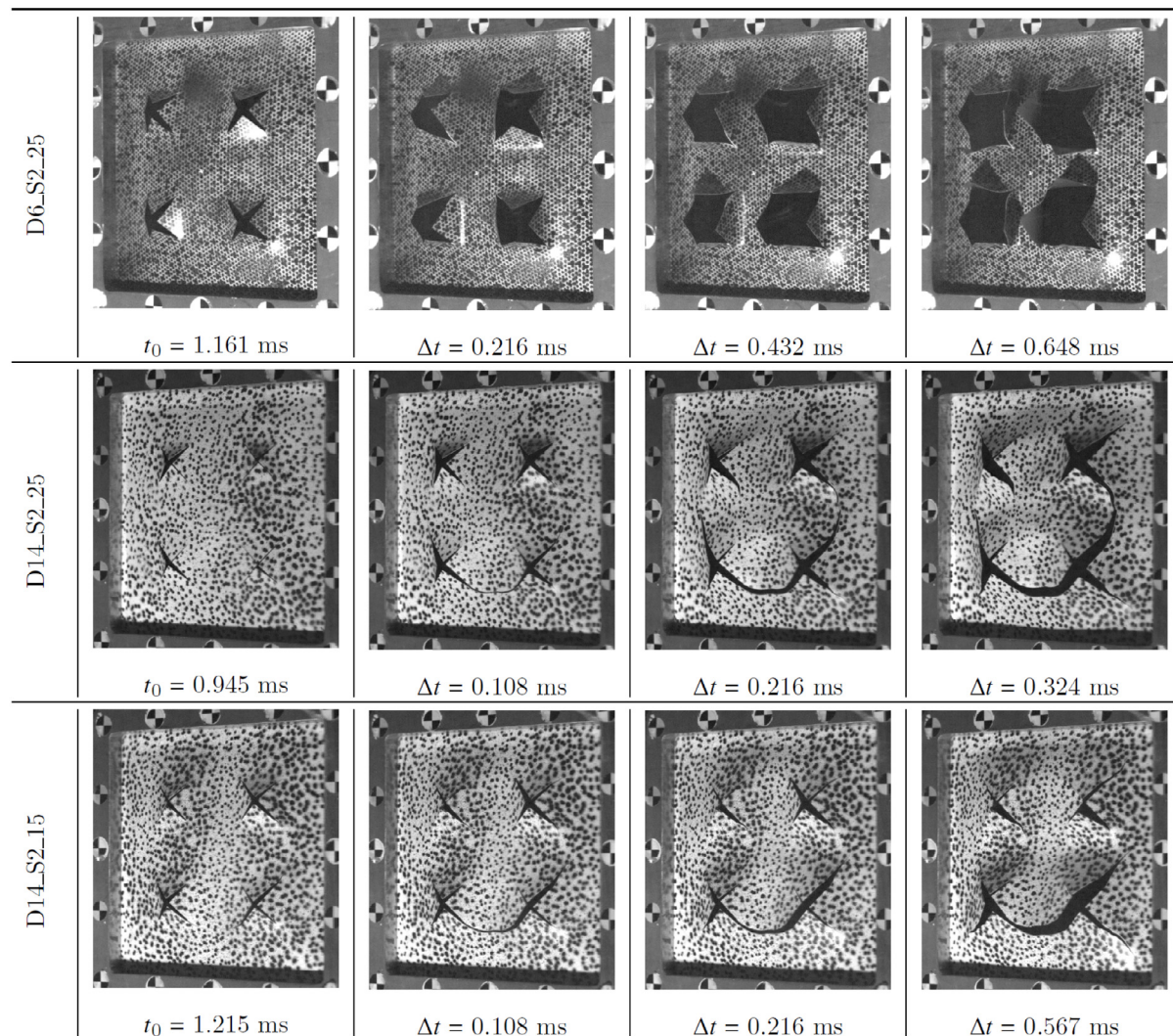
Fig. B.8. Image series of the crack propagation to fracture for the S2 configuration exposed to blast intensities corresponding to firing pressures of 15 bar and 25 bar, for both materials. The given time for the images refers to the same time axis as the pressure plots, i.e., $t_0 = 0$ is defined as when the blast wave is passing the sensor closest to the target plate.

References

[1] M. Ziya-Shamami, H. Babaei, T.M. Mostofi, H. Khodarahmi, Structural response of monolithic and multi-layered circular metallic plates under repeated uniformly distributed impulsive loading: An experimental study, Thin-Walled Struct. 157 (2020) 107024.

[2] G. Langdon, A. Curry, A. Siddiqui, Improving the impulse transfer and response characteristics of explosion loaded compound angle V-plates, Thin-Walled Struct. 148 (2020) 106609.

[3] R. Qi, G.S. Langdon, T.J. Cloete, C.K. Yuen, Behaviour of a blast-driven ball bearing embedded in rear detonated cylindrical explosive, Int. J. Impact Eng. 146 (2020) 103698.

[4] S. Clarke, S. Rigby, S. Fay, A. Barr, A. Tyas, M. Gant, I. Elgy, Characterisation of buried blast loading, Proc. R. Soc. A 476 (2020) 20190791.

[5] X. Jiang, W. Zhang, D. Li, T. Chen, Y. Tang, Z. Guo, Experimental analysis on dynamic response of pre-cracked aluminium plate subjected to underwater explosion shock loadings, Thin-Walled Struct. 159 (2021) 107256.

[6] J. Zhu, Y. Zheng, W. Li, Y. Yang, X. Wang, X. Qiao, L. Xiangxin, R. Li, Axial distribution of fragments from the dynamic explosion fragmentation of metall shells, Int. J. Impact Eng. 123 (2019) 140–146.

[7] K. Hu, G. Chen, C. Zhou, G. Reniers, S. Qi, Z. Zhou, Dynamic response of a large vehicle tank impacted by blast fragments from chemical equipment, Saf. Sci. 130 (2020) 104863.

[8] H.Y. Grisaro, A.N. Dancygier, Characteristics of combined blast and fragments loading, Int. J. Impact Eng. 116 (2018) 51—64.

[9] D. Hyde, U.A.E.W.E. Station, U.S.A.C. of Engineers, User's Guide for Microcomputer Programs ConWep and FunPro, Applications of TM 5-855-1, "Fundamentals of Protective Design for Conventional Weapons", Instruction Report, U.S. Army Engineer Waterways Experiment Station, 1988, URL https://books.google.no/books?id=xHxHAAAACAAJ.

[10] U. Nyström, K. Gylltoft, Numerical studies of the combined effects of blast and fragment loading, Int. J. Impact Eng. 36 (2009) 995—1005.

[11] W. Wilkinson, D. Cormie, M. Arkinstall, Calculation of blast loads for design against terrorism, Proc. Inst. Civ. Eng. - Eng. Comput. Mech. 166 (2013) 132–139.

[12] J. Leppänen, Experiments and numerical analyses of blast and fragment impacts on concrete, Int. J. Impact Eng. 31 (7) (2005) 843–860.

[13] H.Y. Grisaro, A.N. Dancygier, Dynamic response of RC elements subjected to combined loading of blast and fragments, J. Struct. Eng. 147 (2020) 04020315.

[14] P.D. Linz, S.C. Fan, C.K. Lee, Modeling of combined impact and blast loading on reinforced concrete slabs, Lat. Am. J. Solids Struct. 13 (2016) 2266–2282.

[15] P.D. Linz, T.C. Fung, C.K. Lee, W. Riedel, Response mechanisms of reinforced concrete panels to the combined effect of close-in blast and fragments: An integrated experimental and numerical analysis, Int. J. Prot. Struct. 12 (1) (2021) 49–72.

[16] K. Rakvåg, N. Underwood, G. Schleyer, T. Børvik, O. Hopperstad, Transient pressure loading of clamped metallic plates with pre-formed holes, Int. J. Impact Eng. 53 (2012) 44—55.

[17] L. Li, Q.-C. Zhang, R. Zhang, X. Wang, Z.-Y. Zhao, S.-Y. He, B. Han, T.J. Lu, A laboratory experimental technique for simulating combined blast and impact loading, Int. J. Impact Eng. 134 (2019) 103382.

[18] W. Li, P. Wang, G.-P. Feng, Y.-G. Lu, J.-Z. Yue, H.-M. Li, The deformation and failure mechanism of cylindrical shell and square plate with pre-formed holes under blast loading, Def. Technol. 17 (2021) 1143—1159.

[19] Y. Li, W. Wu, H. Zhu, ZhenWua, Z. Dub, The influence of different pre-formed holes on the dynamic response of square plates under air-blast loading, Eng. Fail. Anal. 78 (2017) 122—133.

[20] V. Aune, G. Valsamos, F. Casadei, M. Langseth, T.B. rvik, On the dynamic response of blast-loaded steel plates with and without pre-formed holes, Int. J. Impact Eng. 108 (2017) 27—46.

[21] V. Aune, E. Fagerholt, M. Langseth, T. Børvik, A shock tube facility to generate blast loading on structures, Int. J. Prot. Struct. 7 (2016) 340—366.

[22] V. Aune, E. Fagerholt, K. Hauge, M. Langseth, T.B. rvik, Experimental study on the response of thin aluminium and steel plates subjected to airblast loading, Int. J. Impact Eng. 90 (2016) 106—121.

[23] T. Fras, C.C. Roth, D. Mohr, Fracture of high-strength armour steel under impact loading, Int. J. Impact Eng. 111 (2018) 147–164.

[24] T.B. rvik, S. Dey, A.H. Clausen, Perforation resistance of five different high-strength steel plates subjected to small-arms projectiles, Int. J. Impact Eng. 36 (2009) 948–964.

[25] G.S. Langdon, W.C. Lee, L.A. Louca, The influence of material type on the response of plates to air-blast loading, Int. J. Impact Eng. 78 (2017) 150—160.

[26] B. McDonald, H. Bornstein, G. Langdon, R. Curry, A. Daliri, A. Orifici, Experimental response of high strength steels to localised blast loading, Int. J. Impact Eng. 115 (2018) 106–119.

[27] Y. Wei, Y. Li, L. Zhu, Y. Liu, X. Lei, G. Wang, Y. Wu, Z. Mi, J. Liu, H. Wang, H. Gao, Evading the strength–ductility trade-off dilemma in steel through gradient hierarchical nanotwins, Nature Commun. 5 (2014) 3580, http://dx.doi.org/10.1038/ncomms4580.

[28] J.K. Holmen, J. Johnsen, O. Hopperstad, T. Bø rvik, Influence of fragmentation on the capacity of aluminum alloy plates subjected to ballistic impact, Eur. J. Mech. A Solids 55 (2016) 221–233, http://dx.doi.org/10.1016/j.euromechsol.2015.09.009.

[29] H. Granum, V. Aune, T.B. rvik, O.S. Hopperstad, Effect of heat-treatment on the structural response of blast-loaded aluminium plates with pre-cut slits, Int. J. Impact Eng. 132 (2019) 103306.

[30] C.O. Paulsen, Experimental Characterization of Two-Phase Steels, (Ph.D. thesis), Department of Materials Science and Engineering, NTNU, 2019.

[31] Swedish Steel A.B. (SSAB), 2020, https://www.ssab.com/products/brands/docol (Accessed 13 July 2021), Online.

[32] G. Gruben, M. Langseth, E. Fagerholt, O. Hopperstad, Low-velocity impact on high-strength steel sheets: An experimental and numerical study, Int. J. Impact Eng. 88 (2016) 153—171.

[33] E. Fagerholt, Field Measurements in Mechanical Testing Using Close-Range Photo-Grammetry and Digital Image Analysis, (Ph.D. thesis), NTNU, Norwegian University of Science and Technology, 2012.

[34] J.K. Holmen, O.S. Hopperstad, T.B. rvik, Low-velocity impact on multi-layered dual-phase steel plates, Int. J. Impact Eng. 78 (2017) 161—177.

[35] E. Fagerholt, Online, https://www.ntnu.edu/kt/ecorr (Accessed 13 July 2021).

[36] V. Aune, G. Valsamos, F. Casadei, M. Langseth, T.B. rvik, Fluid-structure interaction effects during the dynamic response of clamped thin steel plates exposed to blast loading, Int. J. Mech. Sci. 195 (2021) 106263.

[37] R. Ritchie, The conflicts between strength and toughness, Nature Mater. 10 (2011) 817–822, http://dx.doi.org/10.1038/nmat3115.